

Topological Quantum Batteries

Zhi-Guang Lu ¹, Guoqing Tian,¹ Xin-You Lü,^{1,*} and Cheng Shang ^{2,3,†}

¹*School of Physics, Huazhong University of Science and Technology, Wuhan, 430074, People's Republic of China*

²*Department of Physics, The University of Tokyo, 5-1-5 Kashiwanoha, Kashiwa, Chiba 277-8574, Japan*

³*Analytical quantum complexity RIKEN Hakubi Research Team,*

RIKEN Center for Quantum Computing (RQC), 2-1 Hirosawa, Wako, Saitama 351-0198, Japan

(Dated: August 14, 2024)

We propose an innovative design for quantum batteries (QBs) that involves coupling two-level systems to a topological photonic waveguide. Employing the resolvent method, we analytically explore the thermodynamic performances of QBs. First, we demonstrate that in the long-time limit, only bound states significantly contribute to the stored energy of QBs. We observe that near-perfect energy transfer can occur in the topologically nontrivial phase. Moreover, the maximum stored energy exhibits singular behavior at the phase boundaries, where the number of bound states undergoes a transition. Second, when a quantum battery and a quantum charger are coupled at the same sublattice within a unit cell, the ergotropy becomes immune to dissipation at that location, facilitated by a dark state and a topologically robust dressed bound state. Third, we show that as dissipation intensifies along with the emergence of the quantum Zeno effect, the charging power of QBs experiences a temporary boost. Our findings offer valuable guidance for improving quantum battery performance through structured reservoir engineering.

Introduction.— With the decline of fossil fuels and the worsening of the global energy crisis, conventional chemical batteries that charge and discharge through chemical reactions will gradually be phased out. Instead, driven by the potential power of quantum effects and the demands for nanotechnological miniaturization, the size of energy storage and conversion devices has shrunk to atomic scales. With this background, Alicki and Fannes first proposed the concept of quantum battery (QB) in 2013 [1]. Fundamentally distinct from conventional batteries, quantum batteries (QBs) exploit unique quantum features for energy storage and release, potentially outperforming classical counterparts with enhanced charging power [2–13], increased capacity [14–18], and superior work extraction [19–24]. Since then, a variety of possible QBs have been constructed, including Dicke type, spin chain type, central-spin type, etc [25–37]. In particular, a minimal yet favorite QB model based on a two-level system has been extensively studied both in theory [38–43] and experimental implementation [44–47].

From an engineering perspective, QBs offer a practical way to incorporate quantum effects into thermodynamics [48–52]. Extensive studies have focused on the performance of QBs in terms of their charging power and stored energy. Notably, the concept of ergotropy—another crucial performance indicator for QBs that describes the maximum extractable energy—was introduced by Allahverdyan, Balian, and Nieuwenhuizen [53]. Very recent research indicates that coupling a QB and a quantum charger to a reservoir, such as a rectangular hollow metal waveguide, facilitates efficient remote charging of the QB but inevitably results in low stored energy and diminished ergotropy [54–56]. A related challenge is whether a structured reservoir exists that can effectively enhance the stored energy and the ergotropy of QBs. Inspired

by the advantages of topological waveguide [57–60] and building on recent experimental advancements [61–75], we have proposed a scheme in this work that enhances the stored energy and the ergotropy by coupling two-level systems (TLSs) with topological photonic waveguide to fully overcome this challenge. Towards implementing QB in practical applications, another natural obstacle is environment-induced decoherence caused by inevitable dissipation, which in general, decreases the performance of the QB, such as the energy loss and aging of QB [76–81]. Recently, the study of QB dynamics in the presence of an environment has attracted a deal of attention, and several schemes have been proposed to mitigate the effects of decoherence, including feedback control [82], exploiting non-Markovian effects [83, 84], Floquet engineering [85], etc. However, does a configuration exist that can completely isolate the QB from the effects of dissipation? Our work offers a substantial answer. We have discovered that directly coupling the quantum charger and QB enables the performance of the QB to resist decoherence, stemming from the presence of a dark state and vacancy-like dressed bound state.

In this letter, by leveraging topological properties, we develop a novel design named topological quantum batteries, which consists of TLSs coupled to a topological photonic waveguide. In this setting, we simultaneously address two major challenges related to QBs. One involves achieving near-perfect charging for QBs, and the other focuses on dissipation immunity engineering. Additionally, we demonstrate that the charging power of QBs can be temporarily enhanced as dissipation increases with the emergence of the quantum Zeno effect.

Setup.— As shown in Fig. 1, we begin by considering a quantum charger and a quantum battery (QB) that are linearly coupled, each modeled as a two-level atom.

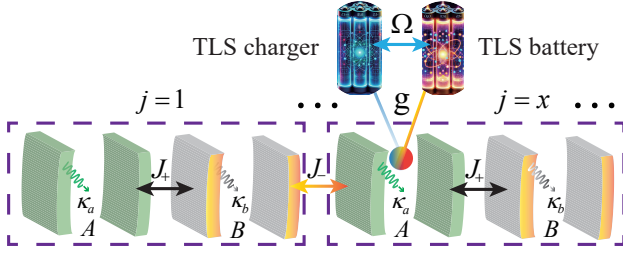


FIG. 1. Configuration illustration of the topological quantum battery (QB). The quantum charger and the QB, formed by linearly interacting two-level systems (TLSs), are coupled to a one-dimensional topological photonic waveguide.

These two-level systems (TLSs) are connected to a one-dimensional Su–Schrieffer–Heeger (SSH) [86, 87] photonic lattice designed with engineered photon loss [88–91]. Under the Markovian and rotating-wave approximations [92], the equation of motion (in the rotating frame and with $\hbar = 1$ here and hereafter) reads

$$\dot{\hat{\rho}}_t = -i \left[\hat{H}_{\text{sys}} + \hat{H}_{\text{ssh}} + \hat{H}_{\text{int}}, \hat{\rho}_t \right] + \mathcal{L}_a \hat{\rho}_t + \mathcal{L}_b \hat{\rho}_t, \quad (1)$$

where

$$\hat{H}_{\text{sys}} = \Delta (\hat{\sigma}_z^B + \hat{\sigma}_z^C) / 2 + \Omega_{12}^{\alpha\beta} (\hat{\sigma}_+^B \hat{\sigma}_-^C + \text{H.c.}), \quad (2)$$

$$\hat{H}_{\text{ssh}} = \sum_{j=1}^N \left(J_+ \hat{a}_j^\dagger \hat{b}_j + J_- \hat{b}_j^\dagger \hat{a}_{j+1} + \text{H.c.} \right), \quad (3)$$

$$\hat{H}_{\text{int}} = g \left(\hat{\sigma}_-^B \hat{\sigma}_{x_1, \alpha}^\dagger + \hat{\sigma}_-^C \hat{\sigma}_{x_2, \beta}^\dagger + \text{H.c.} \right), \quad (4)$$

with $\Omega_{12}^{\alpha\beta} = \Omega \delta_{x_1, x_2} \delta_{\alpha, \beta}$, which implies that the TLSs are directly coupled with strength Ω only when in the same lattice. The Hamiltonian (2) describes a linear coupling between two TLSs, with a detuning Δ between the atomic transition frequency and the lattice resonance frequency, under the assumption that the frequency of each lattice is identical. The Hamiltonian (3) represents a structured bosonic bath with intracell hopping J_+ and intercell hopping J_- , where $J_\pm = J(1 \pm \delta)$. When δ is less (more) than zero, the bath supports topologically non-trivial (trivial) phase. Note that we consider a periodic boundary condition $\hat{a}_{N+1} = \hat{a}_1$. The Hamiltonian (4) gives the atom-bath interaction with a coupling strength of g , where $\hat{\sigma}_+^B$ ($\hat{\sigma}_+^C$) and $\hat{\sigma}_-^B$ ($\hat{\sigma}_-^C$) denote the raising and lowering Pauli operators of QB (quantum charger), respectively. Here, \hat{a}_j^\dagger (\hat{a}_j) or \hat{b}_j^\dagger (\hat{b}_j) are the creation (annihilation) operators of the sublattices A or B at the j th unit cell, and for $\hat{\sigma}_{x_j, \alpha(\beta)}$ with $\alpha(\beta) \in \{A, B\}$, there are $\hat{\sigma}_{x_j, A} \equiv \hat{a}_{x_j}$ and $\hat{\sigma}_{x_j, B} \equiv \hat{b}_{x_j}$. The photon dissipators of different sublattices are given by $\mathcal{L}_a = \kappa_a \sum_j \mathcal{D}[\hat{a}_j]$ and $\mathcal{L}_b = \kappa_b \sum_j \mathcal{D}[\hat{b}_j]$, where κ_a (κ_b) controls the photon loss rates of sublattice A (B), and $\mathcal{D}[\hat{L}]\hat{\rho} = \hat{L}\hat{\rho}\hat{L}^\dagger - \{\hat{L}^\dagger\hat{L}, \hat{\rho}\}/2$ is the Lindblad superoperator.

The effective non-Hermitian (NH) Hamiltonian we obtain from Eq. (1) is given by $\hat{H}_{\text{eff}} = \hat{H}_{\text{sys}} + \hat{H}_{\text{ssh}}^{\text{eff}} + \hat{H}_{\text{int}}$, where $\hat{H}_{\text{ssh}}^{\text{eff}} = \hat{H}_{\text{ssh}} - (i/2) \sum_j (\kappa_a \hat{a}_j^\dagger \hat{a}_j + \kappa_b \hat{b}_j^\dagger \hat{b}_j)$. We suppose that the initial state is in the single-excitation sector. To be specific, the quantum charger is fully charged to the excited state, whereas the QB is depleted to the ground state. Additionally, the bath is in the vacuum state. Then, the solution to Eq. (1) reads $\hat{\rho}_t = e^{-i\hat{H}_{\text{eff}}t} \hat{\rho}_0 e^{i\hat{H}_{\text{eff}}^\dagger t} + p_t |g, g; \text{vac}\rangle \langle g, g; \text{vac}|$ with $p_t = 1 - \text{Tr}[e^{-i\hat{H}_{\text{eff}}t} \hat{\rho}_0 e^{i\hat{H}_{\text{eff}}^\dagger t}]$ [93], in which the initial density matrix is written as $\hat{\rho}_0 = |\psi(0)\rangle \langle \psi(0)|$ with $|\psi(0)\rangle = |e, g; \text{vac}\rangle$. Therefore, by limiting our analysis to the single-excitation sector, we can concentrate on studying the effective NH Hamiltonian. Further, by defining $\hat{\mathbf{o}}_k = [\hat{a}_k, \hat{b}_k]^T$ with $\hat{a}_k^\dagger = \sum_{j=1}^N e^{ikj} \hat{a}_j^\dagger / \sqrt{N}$ and $\hat{b}_k^\dagger = \sum_{j=1}^N e^{ikj} \hat{b}_j^\dagger / \sqrt{N}$, where $k = 2\pi n/N$ for $n \in (-N/2, N/2]$ within a lattice of cell size N , the effective Hamiltonian of the bath, $\hat{H}_{\text{ssh}}^{\text{eff}}$, when moved to the momentum space, is expressed as $\sum_k \hat{\mathbf{o}}_k^\dagger \tilde{\mathbf{h}}_k \hat{\mathbf{o}}_k$, with [93]

$$\tilde{\mathbf{h}}_k = \text{Re}[f_k] \sigma_x - \text{Im}[f_k] \sigma_y - i\kappa_- \sigma_z - i\kappa_+ \sigma_0, \quad (5)$$

where $f_k = J_+ + J_- e^{-ik}$ is the coupling in momentum space between the bosonic modes of \hat{a}_k and \hat{b}_k , and $\kappa_\pm = (\kappa_a \pm \kappa_b)/4$. Then, by incorporating Eq. (5) and applying the definitions of \hat{a}_k and \hat{b}_k , we can obtain the generalized NH effective Hamiltonian expressed in momentum space.

Dynamics.— Let us move on to study the dynamics of the QB. Specifically, we focus on the nonunitary evolution $|\psi(t)\rangle = e^{-i\hat{H}_{\text{eff}}t} |\psi(0)\rangle$ starting from the initial state, $|\psi(0)\rangle = |e, g; \text{vac}\rangle$ of the total system, for which the quantum charger is fully charged while the QB is empty, where $|\text{vac}\rangle$ denotes the vacuum state of the lattice of bosonic modes. To analytically solve the dynamics of the QB in this scenario, we assume that the bath is in the thermodynamic limit ($N \rightarrow \infty$). By using the resolvent method [94, 95], the probability amplitude for the QB to be excited at any time can be calculated [93]

$$c_B(t) = \int_{\mathcal{C}} \frac{dz}{2\pi i} \frac{\Sigma_{12}^{\alpha\beta}(z) + \Omega_{12}^{\alpha\beta}}{\mathcal{D}(z)} e^{-izt}, \quad (6)$$

where $\Sigma_{mn}^{\alpha\beta}(z) = g^2 G(x_{m,\alpha}, x_{n,\beta}; z)$ refers to the self-energy of TLSs. The single-particle Green’s function of the bath is denoted as $G(x_{m,\alpha}, x_{n,\beta}; z) = \langle \text{vac} | \hat{\sigma}_{x_{m,\alpha}}(z - \sum_k \hat{\mathbf{o}}_k^\dagger \tilde{\mathbf{h}}_k \hat{\mathbf{o}}_k)^{-1} \hat{\sigma}_{x_{n,\beta}}^\dagger | \text{vac} \rangle$, and $\mathcal{D}(z) = [z - \Delta - \Sigma_{11}^{\alpha\alpha}(z)][z - \Delta - \Sigma_{22}^{\beta\beta}(z)] - [\Omega_{12}^{\alpha\beta} + \Sigma_{12}^{\alpha\beta}(z)]^2$.

Bound state.— Now, we introduce the bound state, a critical “hidden” physical quantity impacting QB performance. By precisely solving the probability amplitude in Eq. (6), we find that the time evolution of the TLSs is fully contributed by three parts: the bound state energies (BSEs), branch-cut detours, and unstable poles. Since the contributions from the branch-cut detours and

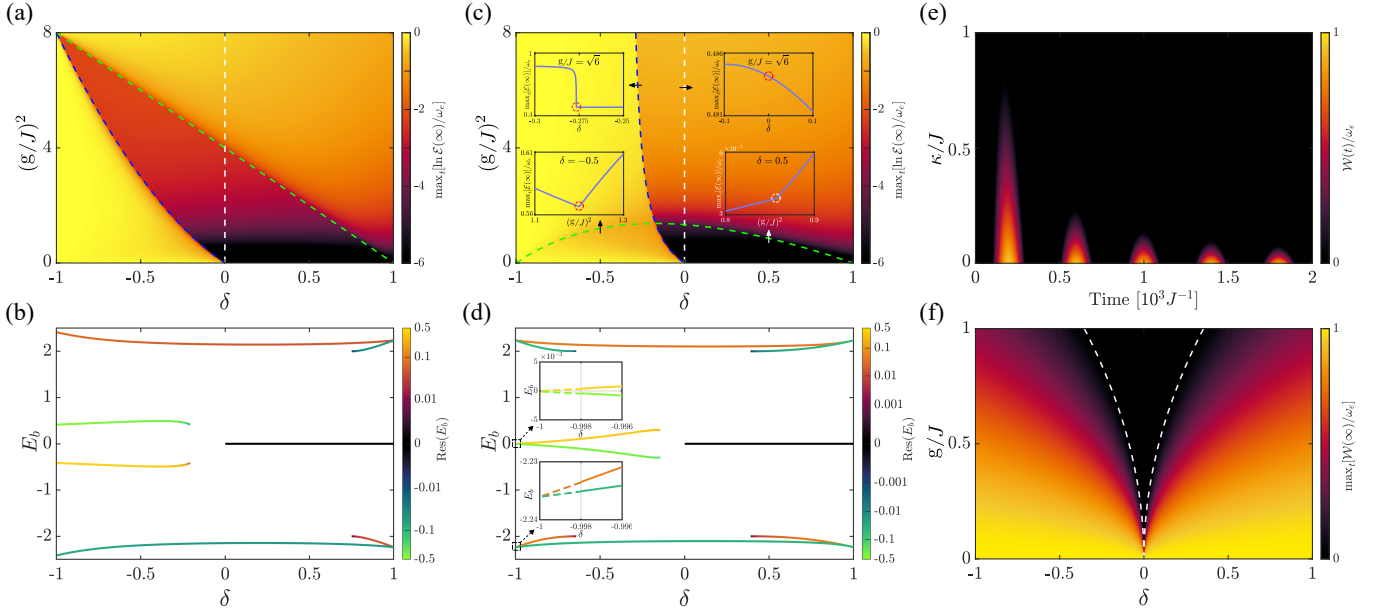


FIG. 2. Panels (a) and (c) describe the maximum stored energy $\max_t [\mathcal{E}(\infty)]$ as a function of the dimerization parameter δ and the atom-bath coupling strength g , for $d = -1$ and $d = -2$ respectively. The white dashed line represents the topological phase boundary of the bath ($\ell_0 : \delta = 0$), while the blue and green dashed lines, ℓ_1 and ℓ_2 , respectively, represent two phase boundaries of the MSE. In panel (c), the two insets at the bottom exhibit singular behavior of the MSE at $\delta = \pm 0.5$ upon crossing phase boundary ℓ_2 . Panels (b) and (d) show the BSEs vary with δ at $d = -1$ and $d = -2$, respectively. The residues at the BSEs are color-coded, facilitating observation of the contribution in Eq. (7) of these bound states. Panel (e) shows how dissipation κ affects the ergotropy $\mathcal{W}(t)$ of QB varies over time with the other parameters are set to $g/J = 0.1$, $\delta = -0.26$, and $d = -1$. For (a)-(e) the other parameters are chosen as $\Delta = 0$, $\alpha = B$, and $\beta = A$. Panel (f) shows the maximum ergotropy $\max_t [\mathcal{W}(\infty)]$ as a function of δ and g with the other parameters are set to $\Delta = -\Omega = \kappa = J$, $\alpha = \beta = A$, and $d = 0$. The white dashed curve, defined by the equation $(g/J)^2 = 2\sqrt{2}|\delta|$, depicts the boundaries where $\max_t [\mathcal{W}(\infty)] = 0$. Here, we consider a dissipation-free bath (i.e., $\kappa_a = \kappa_b = 0$) for (a)-(d) and a single-sublattice dissipative bath (i.e., $\kappa_a \equiv \kappa$ and $\kappa_b = 0$) for (e)-(f), and set $g/J = 1$ for both (b) and (d).

the unstable poles decay quickly over time, only the BSEs survive in the long-time limit, and we obtain [93]

$$c_B(\infty) = \sum_{z_k \in E_b} \text{Res} \left[\frac{\Sigma_{12}^{\alpha\beta}(z) + \Omega_{12}^{\alpha\beta}}{\mathcal{D}(z)}, z_k \right] e^{-iz_k t}, \quad (7)$$

where E_b represents the BSEs [96], i.e., the completely real eigenenergies of the bound states, which can be obtained by solving the real roots of the pole equation $\mathcal{D}(E_b) = 0$, or equivalently, by imposing the eigenstate condition $\hat{H}_{\text{eff}} |\psi_b\rangle = E_b |\psi_b\rangle$. Henceforth, we denote the residue in Eq. (7) as $\text{Res}(z_k)$, defined as $\text{Res}\{\Sigma_{12}^{\alpha\beta}(z) + \Omega_{12}^{\alpha\beta}/\mathcal{D}(z), z_k\}$.

QB performance indicators.— Next, to quantify the performance of QBs, we introduce three crucial thermodynamic indicators, starting with the stored energy. The energy of the QB at time t is defined as

$$\mathcal{E}(t) = \text{Tr} [\hat{\rho}_B(t) \hat{H}_B] = \omega_e |c_B(t)|^2, \quad (8)$$

where $\hat{H}_B = \omega_e \sigma_+^B \sigma_-^B$ describes the Hamiltonian of the QB with a characteristic frequency ω_e , while $\hat{\rho}_B(t)$ denotes the reduced density matrix of the QB.

Based on the stored energy, we can define the second thermodynamic indicator, the charging power of the QB, as $P(t) = \mathcal{E}(t)/t$, its performance will be discussed later.

The third key indicator is called ergotropy, which is used to describe the maximum energy that can be extracted at time t , defined by

$$\mathcal{W}(t) = \text{Tr} [\hat{\rho}_B(t) \hat{H}_B] - \text{Tr} [\hat{\rho}_B(t) \hat{H}_B], \quad (9)$$

where $\hat{\rho}_B(t) = \sum_s r_s(t) |\varepsilon_s\rangle \langle \varepsilon_s|$ is the passive state, $r_s(t)$ are the eigenvalues of $\hat{\rho}_B(t)$ arranged in descending order, while $|\varepsilon_s\rangle$ are the eigenstates of \hat{H}_B with the corresponding eigenvalues ε_s sorted in ascending order.

QB phase diagram.— By substituting Eq. (7) into Eq. (8), we demonstrate that the stored energy of the QB in the long-time limit is only determined by the contributions of BSEs. Thus, both the value of the BSEs and their corresponding residues are essential for QB performance. In Figs. 2(a) and 2(c), we observe that under resonance conditions ($\Delta = 0$), the maximum stored energy (MSE) of the QB varies across different unit cell distances ($d = x_1 - x_2 < 0$) between the quantum charger and QB, exhibiting a singular behavior (derivative discontinuity)

precisely at the phase boundaries [93]

$$\ell_1: |g| = 2\sqrt{\frac{\delta(1-\delta^2)J^2}{\delta(1+2d)-1}}; \ell_2: |g| = 2\sqrt{\frac{(1-\delta^2)J^2}{\delta-1-2d}}. \quad (10)$$

Specifically, this behavior arises from a jump in the number of bound states at phase boundaries and the corresponding discontinuity in their residues. However, despite such jumps at the topological phase boundary, the MSE remains continuous at the boundary [see the insets in Fig. 2(c)] due to the vanishing residue of degenerate zero-energy bound states [93]. Notably, in the parameter region to the left of phase boundary ℓ_1 , most of the energy from the quantum charger is successfully transferred to the QB. Conversely, energy transmission is nearly completely obstructed to the right of this boundary. Physically, whether the charging process proceeds smoothly depends on the spatial distribution of bound states on sublattices A and B . In the Markovian region ($g \ll J$), for the topologically trivial phase ($\delta > 0$), there is no overlap in the spatial distribution of bound states, leading to an almost complete shutdown of energy transfer. In contrast, for the topologically non-trivial phase ($\delta < 0$), the spatial distribution of bound states overlaps, allowing the energy in the quantum charger to be fully transferred to the QB. Additionally, we also observe that at $d = -1$ and $d = -2$, the intersection point of phase boundaries (ℓ_1 and ℓ_2) has shifted, significantly expanding the parameter region for optimal energy transmission, i.e., the region is located to the left of the phase boundary ℓ_1 , and the intersection point can be determined using Eq. (10). It is important to note that at the critical point $\delta = -1$, the QB and quantum charger decouple as long as $d \neq -1$, halting the charging process, while near this critical point, the energy of the quantum charger can be transferred almost completely to the QB, as depicted in the insets of Fig. 2(d).

QB dissipation immunity.— As shown in Fig. 2(e), for $\Omega_{12}^{\alpha\beta} = 0$ (without direct coupling), we plot the ergotropy (9) of the QB as a function of dissipation $\kappa_a \equiv \kappa$ and time. We observe that dissipation causes a decrease in the ergotropy of the QB and that increasing the dissipation rate further accelerates this decline. Specifically, when $\kappa > 0$, $\mathcal{W}(\infty) = 0$. For $\Omega_{12}^{\alpha\beta} \neq 0$, we are surprised to find that as long as condition $\Delta = -\Omega$ is met, even if the direct coupling between the quantum charger and QB is extremely weak, the QB is still immune to direct dissipation κ . This is evident from the analytical expression [93]

$$\frac{\max_t [\mathcal{W}(\infty)]}{\omega_e} = \frac{4J^4\delta^2 - g^4/2}{(2J^2|\delta| + g^2)^2} \Theta\left(2^{\frac{3}{4}}J\sqrt{|\delta|} - |g|\right) \quad (11)$$

of the maximum ergotropy for $\Delta = -\Omega$ in the long-time limit, showing that it is independent of κ . This result applies exclusively to topological photonic waveguides. Physically, when the condition $\Delta \neq \Omega$ is met,

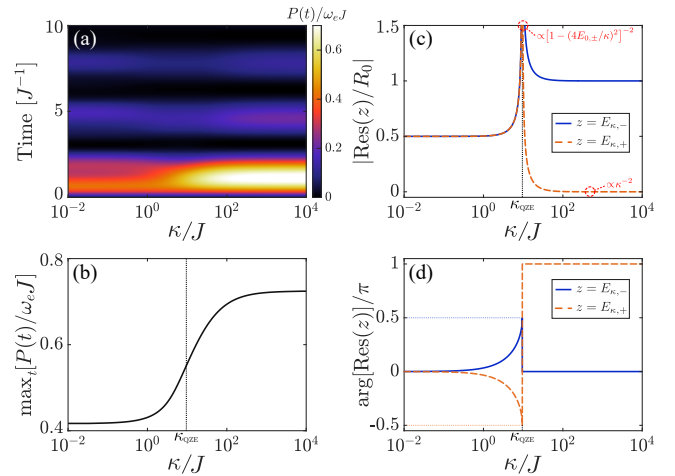


FIG. 3. (a) Charging power $P(t)$ as a function of dissipation κ and time t . The maximum charging power $\max_t [P(t)]$ corresponding to (a) varies with κ as shown in (b). (c) and (d) respectively represent the modulus $|\text{Res}(z)|$ and the phase $\arg[\text{Res}(z)]$ of the residue at the dissipative BSEs ($E_{\kappa,\pm}$) as they vary with κ , which $E_{\kappa,-}$ and $E_{\kappa,+}$ are represented by the blue solid line and the orange dashed line, respectively. The critical point for the occurrence of the quantum Zeno effect is marked as κ_{QZE} . The parameters for (a)-(d) are chosen as $\Delta = -\Omega = J$, $g/J = 1$, and $\delta = 0.9$.

there always exists a superposition called dark state [97], while when the condition $\Delta = -\Omega$ also holds, a hidden non-degenerate zero-energy bound state emerges, termed a vacancy-like dressed bound state [98], also known as a topologically robust dressed bound state in an SSH model. As a result, the involvement of these two bound states renders the performance of QB immune to sublattice dissipation from the bath. Additionally, we emphasize that the strong robustness of vacancy-like dressed bound states against disorder contributes to the performance of the QB in resisting the effects of disorder [93].

QB performance boost in short time.— To assess the performance of QBs, it is crucial to consider not only the stored energy and the ergotropy as key physical quantities but also the charging power as an indispensable indicator. Since the energy storage of a QB composed of a TLS is bounded, i.e., $0 \leq \mathcal{E}(t) \leq \omega_e$, the charging power of QB inevitably approaching zero in the long-time limit. Thus, discussions on the charging power of QB are primarily focused on short-time regions. Following the configuration of immunity to dissipation over long time limits, we are curious whether it is possible to enhance the charging power by utilizing dissipation in a short time. First, the system is known to contain two bound states immune to dissipation. Second, two additional bound states exist for the dissipation-free bath, whose energies are $E_{0,\pm}$. Further, when dissipation is introduced, these two bound states transform into dissipative bound states with imaginary energy less than zero,

whose energies are [93]

$$E_{\kappa,\pm} = -\frac{i}{4}\kappa \pm \sqrt{E_{0,\pm}^2 - \left(\frac{\kappa}{4}\right)^2}. \quad (12)$$

When $\kappa \gg \kappa_{\text{QZE}} \equiv 4|E_{0,\pm}|$, we find a dramatic change in the lifetimes of the two dissipative bound states, i.e., $\text{Im}[E_{\kappa,+}] \propto -\kappa$ and $\text{Im}[E_{\kappa,-}] \propto -1/\kappa$. Here, we note that the lifetime of the dissipative bound states with energy $E_{\kappa,-}$ is proportional to κ , and thus we may refer to this phenomenon as the quantum Zeno effect [99]. Simultaneously, their corresponding contribution to the residue satisfies $\text{Res}(E_{\kappa,+}) \propto 1/\kappa^2$ and $\text{Res}(E_{\kappa,-}) \approx R_0$, where $R_0 = 2g^4/[E_{0,\pm}^4 - 2J^2(1 + \delta^2)E_{0,\pm}^2]$, and we see that $\text{Res}(E_{\kappa,+})$ significantly decreases as κ increases, while $\text{Res}(E_{\kappa,-})$ remains unchanged. According to Eq. (12), once κ exceeds κ_{QZE} , the energy of the dissipative bound states becomes purely imaginary. Furthermore, as κ increases, the imaginary parts of the energies of these two bound states exhibit opposite trends: one decreases while the other increases. Consequently, we refer to κ_{QZE} as the critical point where the quantum Zeno effect begins to emerge. In Fig. 3(c) and Fig. 3(d), we intuitively observe how both the modulus and the phase of $\text{Res}(E_{\kappa,\pm})$ vary with κ . In Fig. 3(a), we show that when κ is present, the $P(t)$ exhibits a rapid periodic oscillatory decay over time. In a short time scale, i.e., $t \sim \pi/(2|\Omega|)$, increasing κ can be accompanied by enhancing $P(t)$. In Fig. 3(b), we observe that as κ continues to increase and goes beyond κ_{QZE} , the emergence of the quantum Zeno effect leads to a significant increase in $\max_t[P(t)]$. In addition, it is worth mentioning that if we observe the stroboscopic dynamics of the dissipative system at $t = (2\pi\mathbb{Z})/|E_{0,\pm}|$, we should find it nearly identical to the dynamics of a non-dissipative system.

Summary and outlook.— To summarize, we have developed a general framework for analyzing the atomic dynamics of two-level systems coupled to a topological photonic waveguide. First, we have demonstrated that only the contributions from bound state energies are retained in the long-time limits. We have pointed out that topological properties determine the charging process from the quantum charger to the QB, and near-perfect transmission may occur in a topologically non-trivial phase. Moreover, we have discovered that the maximum stored energy exhibits singular behavior at the phase boundary. Second, we have highlighted that even with extremely weak coupling between the quantum charger and the QB, the performance of the QB, such as ergotropy, can resist environment-induced decoherence due to the presence of a dark state and a topologically robust dressed bound state. Third, we have shown that an increase in dissipation significantly enhances the charging power of the QB over a short time due to the emergence of the quantum Zeno effect.

A significant prospect is further exploring the performance of QBs in generalized open quantum sys-

tems. As a concrete example, we will consider a one-dimensional tight-binding model with asymmetric hopping as an environment, investigating the performance of non-Hermitian QBs through the perspective of the Hatano-Nelson model [100]. Additionally, understanding the implicit relation between non-Markovian effects and the alterations in the phase boundary curves within our phase diagram would also be intriguing. Another practical direction for future research may be extending the study of QBs to multi-excitation coherence charging. Specifically, it would be valuable to investigate the performance of multi-excitation [101–103] using numerical techniques such as matrix product states [104] or hierarchical equations of motion analogs [105].

We are grateful to Naomichi Hatano for carefully reading the manuscript. C. Shang thanks Ken-Ichiro Imura, Tomotaka Kuwahara, and Takano Taira for their valuable discussions. C. Shang would also like to thank the committee members in the Ph.D. defense, Yuto Ashida, Masahito Ueda, Mio Murao, Kiyotaka Aikawa, and Kuniaki Konishi, for their careful review and insightful comments. This work is supported by the National Key Research and Development Program of China grant 2021YFA1400700 and the Fundamental Research Funds for the Central Universities (Grant No. 2024BRA001). C. Shang acknowledges the financial support by the China Scholarship Council, the Japanese Government (Monbukagakusho-MEXT) Scholarship under Grant No. 211501, and the RIKEN Junior Research Associate Program.

* xinyoulu@hust.edu.cn

† c-shang@iis.u-tokyo.ac.jp

- [1] R. Alicki and M. Fannes, Entanglement boost for extractable work from ensembles of quantum batteries, *Phys. Rev. E* **87**, 042123 (2013).
- [2] F. Campaioli, F. A. Pollock, F. C. Binder, L. Céleri, J. Goold, S. Vinjanampathy, and K. Modi, Enhancing the charging power of quantum batteries, *Phys. Rev. Lett.* **118**, 150601 (2017).
- [3] S. Seah, M. Perarnau-Llobet, G. Haack, N. Brunner, and S. Nimmrichter, Quantum speed-up in collisional battery charging, *Phys. Rev. Lett.* **127**, 100601 (2021).
- [4] G. Zhu, Y. Chen, Y. Hasegawa, and P. Xue, Charging quantum batteries via indefinite causal order: Theory and experiment, *Phys. Rev. Lett.* **131**, 240401 (2023).
- [5] F. Centrone, L. Mancino, and M. Paternostro, Charging batteries with quantum squeezing, *Phys. Rev. A* **108**, 052213 (2023).
- [6] D. Rossini, G. M. Andolina, D. Rosa, M. Carrega, and M. Polini, Quantum advantage in the charging process of sachdev-ye-kitaev batteries, *Phys. Rev. Lett.* **125**, 236402 (2020).
- [7] J.-Y. Gyhm and U. R. Fischer, Beneficial and detrimental entanglement for quantum battery charging, *AVS Quantum Science* **6** (2023).

- [8] J.-Y. Gyhm, D. Šafránek, and D. Rosa, Quantum charging advantage cannot be extensive without global operations, *Phys. Rev. Lett.* **128**, 140501 (2022).
- [9] D. Rosa, D. Rossini, G. M. Andolina, M. Polini, and M. Carrega, Ultra-stable charging of fast-scrambling syk quantum batteries, *Journal of High Energy Physics* **2020**, 1 (2020).
- [10] C. Rodríguez, D. Rosa, and J. Olle, Artificial intelligence discovery of a charging protocol in a micromaser quantum battery, *Phys. Rev. A* **108**, 042618 (2023).
- [11] F. Mazzoncini, V. Cavina, G. M. Andolina, P. A. Erdman, and V. Giovannetti, Optimal control methods for quantum batteries, *Phys. Rev. A* **107**, 032218 (2023).
- [12] T. K. Konar, L. G. C. Lakkaraju, and A. Sen (De), Quantum battery with non-hermitian charging, *Phys. Rev. A* **109**, 042207 (2024).
- [13] Y.-Y. Zhang, T.-R. Yang, L. Fu, and X. Wang, Powerful harmonic charging in a quantum battery, *Phys. Rev. E* **99**, 052106 (2019).
- [14] X. Yang, Y.-H. Yang, M. Alimuddin, R. Salvia, S.-M. Fei, L.-M. Zhao, S. Nimmrichter, and M.-X. Luo, Battery capacity of energy-storing quantum systems, *Phys. Rev. Lett.* **131**, 030402 (2023).
- [15] S. Julià-Farré, T. Salamon, A. Riera, M. N. Bera, and M. Lewenstein, Bounds on the capacity and power of quantum batteries, *Phys. Rev. Res.* **2**, 023113 (2020).
- [16] L. Gao, C. Cheng, W.-B. He, R. Mondaini, X.-W. Guan, and H.-Q. Lin, Scaling of energy and power in a large quantum battery-charger model, *Phys. Rev. Res.* **4**, 043150 (2022).
- [17] T. Zhang, H. Yang, and S.-M. Fei, Local-projective-measurement-enhanced quantum battery capacity, *Phys. Rev. A* **109**, 042424 (2024).
- [18] S. Tirone, R. Salvia, S. Chessa, and V. Giovannetti, Quantum work capacitances: ultimate limits for energy extraction on noisy quantum batteries, [arXiv:2211.02685](https://arxiv.org/abs/2211.02685) (2024).
- [19] H.-L. Shi, S. Ding, Q.-K. Wan, X.-H. Wang, and W.-L. Yang, Entanglement, coherence, and extractable work in quantum batteries, *Phys. Rev. Lett.* **129**, 130602 (2022).
- [20] G. M. Andolina, M. Keck, A. Mari, M. Campisi, V. Giovannetti, and M. Polini, Extractable work, the role of correlations, and asymptotic freedom in quantum batteries, *Phys. Rev. Lett.* **122**, 047702 (2019).
- [21] G. Francica and L. Dell'Anna, Optimal work extraction from quantum batteries based on the expected utility hypothesis, *Phys. Rev. E* **109**, 044119 (2024).
- [22] J. Monsel, M. Fellous-Asiani, B. Huard, and A. Auffèves, The energetic cost of work extraction, *Phys. Rev. Lett.* **124**, 130601 (2020).
- [23] S. Tirone, R. Salvia, S. Chessa, and V. Giovannetti, Work extraction processes from noisy quantum batteries: The role of nonlocal resources, *Phys. Rev. Lett.* **131**, 060402 (2023).
- [24] S. Tirone, R. Salvia, S. Chessa, and V. Giovannetti, Quantum work extraction efficiency for noisy quantum batteries: the role of coherence, [arXiv:2305.16803](https://arxiv.org/abs/2305.16803) (2023).
- [25] D. Ferraro, M. Campisi, G. M. Andolina, V. Pellegrini, and M. Polini, High-power collective charging of a solid-state quantum battery, *Phys. Rev. Lett.* **120**, 117702 (2018).
- [26] D. Rossini, G. M. Andolina, and M. Polini, Many-body localized quantum batteries, *Phys. Rev. B* **100**, 115142 (2019).
- [27] L. Peng, W.-B. He, S. Chesi, H.-Q. Lin, and X.-W. Guan, Lower and upper bounds of quantum battery power in multiple central spin systems, *Phys. Rev. A* **103**, 052220 (2021).
- [28] L. Fusco, M. Paternostro, and G. De Chiara, Work extraction and energy storage in the dicke model, *Phys. Rev. E* **94**, 052122 (2016).
- [29] S. S. Seidov and S. I. Mukhin, Quantum dicke battery supercharging in the bound-luminosity state, *Phys. Rev. A* **109**, 022210 (2024).
- [30] A. Crescente, M. Carrega, M. Sassetti, and D. Ferraro, Ultrafast charging in a two-photon dicke quantum battery, *Phys. Rev. B* **102**, 245407 (2020).
- [31] B. Ahmadi, P. Mazurek, P. Horodecki, and S. Barzanjeh, Nonreciprocal quantum batteries, [arXiv:2401.05090](https://arxiv.org/abs/2401.05090) (2024).
- [32] J. Kim, J. Murugan, J. Olle, and D. Rosa, Operator delocalization in quantum networks, *Phys. Rev. A* **105**, L010201 (2022).
- [33] V. Shaghghi, V. Singh, G. Benenti, and D. Rosa, Micro-masers as quantum batteries, *Quantum Science and Technology* **7**, 04LT01 (2022).
- [34] G. Gemme, G. M. Andolina, F. M. D. Pellegrino, M. Sassetti, and D. Ferraro, Off-resonant dicke quantum battery: Charging by virtual photons, *Batteries* **9**, 040197 (2023).
- [35] G. M. Andolina, P. A. Erdman, F. Noé, J. Pekola, and M. Schirò, Dicke superradiant enhancement of the heat current in circuit qed, [arXiv:2401.17469](https://arxiv.org/abs/2401.17469) (2024).
- [36] T. K. Konar, L. G. C. Lakkaraju, S. Ghosh, and A. Sen(De), Quantum battery with ultracold atoms: Bosons versus fermions, *Phys. Rev. A* **106**, 022618 (2022).
- [37] A. G. Catalano, S. M. Giampaolo, O. Morsch, V. Giovannetti, and F. Franchini, Frustrating quantum batteries, [arXiv:2307.02529](https://arxiv.org/abs/2307.02529) (2023).
- [38] F. C. Binder, S. Vinjanampathy, K. Modi, and J. Goold, Quantacell: powerful charging of quantum batteries, *New Journal of Physics* **17**, 075015 (2015).
- [39] L. P. García-Pintos, A. Hama, and A. del Campo, Fluctuations in extractable work bound the charging power of quantum batteries, *Phys. Rev. Lett.* **125**, 040601 (2020).
- [40] F. H. Kamin, F. T. Tabesh, S. Salimi, and A. C. Santos, Entanglement, coherence, and charging process of quantum batteries, *Phys. Rev. E* **102**, 052109 (2020).
- [41] L. Wang, S.-Q. Liu, F.-I. Wu, H. Fan, and S.-Y. Liu, Two-mode raman quantum battery dependent on coupling strength, *Phys. Rev. A* **108**, 062402 (2023).
- [42] F. H. Kamin, S. Salimi, and M. B. Arjmandi, Steady-state charging of quantum batteries via dissipative ancillas, *Phys. Rev. A* **109**, 022226 (2024).
- [43] A. C. Santos, Quantum advantage of two-level batteries in the self-discharging process, *Phys. Rev. E* **103**, 042118 (2021).
- [44] C. D. Bruzewicz, J. Chiaverini, R. McConnell, and J. M. Sage, Trapped-ion quantum computing: Progress and challenges, *Applied Physics Reviews* **6** (2019).
- [45] P. Forn-Díaz, J. J. García-Ripoll, B. Peropadre, J.-L. Orgiazzi, M. Yurtalan, R. Belyansky, C. M. Wilson, and A. Lupascu, Ultrastrong coupling of a single artificial atom to an electromagnetic continuum in the nonperturbative regime, *Nature Physics* **13**, 39 (2017).
- [46] K. Baumann, C. Guerlin, F. Brennecke, and T. Esslinger, Dicke quantum phase transition with a superfluid gas in an optical cavity, *Nature* **464**, 1301 (2010).
- [47] M. H. Devoret and R. J. Schoelkopf, Superconducting

- circuits for quantum information: an outlook, *Science* **339**, 1169 (2013).
- [48] F. Campaioli, F. A. Pollock, and S. Vinjanampathy, Quantum batteries, *Thermodynamics in the Quantum Regime: Fundamental Aspects and New Directions*, 207 (2018).
- [49] K. Southwell, Quantum coherence., *Nature* **453**, 1003 (2008).
- [50] O. Abah, G. De Chiara, M. Paternostro, and R. Puebla, Harnessing nonadiabatic excitations promoted by a quantum critical point: Quantum battery and spin squeezing, *Phys. Rev. Res.* **4**, L022017 (2022).
- [51] D. Saha, A. Bhattacharyya, K. Sen, and U. Sen, Harnessing energy extracted from heat engines to charge quantum batteries, [arXiv:2309.15634](https://arxiv.org/abs/2309.15634) (2023).
- [52] F. Campaioli, S. Gherardini, J. Q. Quach, M. Polini, and G. M. Andolina, Colloquium: Quantum batteries, [arXiv:2308.02277](https://arxiv.org/abs/2308.02277) (2023).
- [53] A. E. Allahverdyan, R. Balian, and T. M. Nieuwenhuizen, Maximal work extraction from finite quantum systems, *Europhysics Letters* **67**, 565 (2004).
- [54] W.-L. Song, H.-B. Liu, B. Zhou, W.-L. Yang, and J.-H. An, Remote charging and degradation suppression for the quantum battery, *Phys. Rev. Lett.* **132**, 090401 (2024).
- [55] S.-Y. Bai and J.-H. An, Generating stable spin squeezing by squeezed-reservoir engineering, *Phys. Rev. Lett.* **127**, 083602 (2021).
- [56] W. Song, W. Yang, J. An, and M. Feng, Dissipation-assisted spin squeezing of nitrogen-vacancy centers coupled to a rectangular hollow metallic waveguide, *Optics Express* **25**, 19226 (2017).
- [57] W. Nie, T. Shi, F. Nori, and Y.-x. Liu, Topology-enhanced nonreciprocal scattering and photon absorption in a waveguide, *Phys. Rev. Appl.* **15**, 044041 (2021).
- [58] M. Bello, G. Platero, J. I. Cirac, and A. González-Tudela, Unconventional quantum optics in topological waveguide qed, *Science advances* **5**, eaaw0297 (2019).
- [59] C. Tabares, A. Muñoz de las Heras, L. Tagliacozzo, D. Porrás, and A. González-Tudela, Variational quantum simulators based on waveguide qed, *Phys. Rev. Lett.* **131**, 073602 (2023).
- [60] G. Tian, Y. Wu, and X.-Y. Lü, [Power-law-exponential interaction induced quantum spiral phases](https://arxiv.org/abs/2405.14243) (2024), [arXiv:2405.14243 \[quant-ph\]](https://arxiv.org/abs/2405.14243).
- [61] L. Lu, J. D. Joannopoulos, and M. Soljačić, Topological photonics, *Nature photonics* **8**, 821 (2014).
- [62] T. Ozawa, H. M. Price, A. Amo, N. Goldman, M. Hafezi, L. Lu, M. C. Rechtsman, D. Schuster, J. Simon, O. Zilberberg, and I. Carusotto, Topological photonics, *Rev. Mod. Phys.* **91**, 015006 (2019).
- [63] B. M. Anderson, R. Ma, C. Owens, D. I. Schuster, and J. Simon, Engineering topological many-body materials in microwave cavity arrays, *Phys. Rev. X* **6**, 041043 (2016).
- [64] S. Haroche and J.-M. Raimond, *Exploring the Quantum: Atoms, Cavities, and Photons* (Oxford University Press, 2006).
- [65] P. Lodahl, S. Mahmoodian, and S. Stobbe, Interfacing single photons and single quantum dots with photonic nanostructures, *Rev. Mod. Phys.* **87**, 347 (2015).
- [66] D. E. Chang, J. S. Douglas, A. González-Tudela, C.-L. Hung, and H. J. Kimble, Colloquium: Quantum matter built from nanoscopic lattices of atoms and photons, *Rev. Mod. Phys.* **90**, 031002 (2018).
- [67] S. Barik, A. Karasahin, C. Flower, T. Cai, H. Miyake, W. DeGottardi, M. Hafezi, and E. Waks, A topological quantum optics interface, *Science* **359**, 666 (2018).
- [68] S. John and J. Wang, Quantum electrodynamics near a photonic band gap: Photon bound states and dressed atoms, *Phys. Rev. Lett.* **64**, 2418 (1990).
- [69] Y. Liu and A. A. Houck, Quantum electrodynamics near a photonic bandgap, *Nature Physics* **13**, 48 (2017).
- [70] E. Kim, X. Zhang, V. S. Ferreira, J. Banker, J. K. Iverson, A. Sipahigil, M. Bello, A. González-Tudela, M. Mirhosseini, and O. Painter, Quantum electrodynamics in a topological waveguide, *Phys. Rev. X* **11**, 011015 (2021).
- [71] N. M. Sundaresan, R. Lundgren, G. Zhu, A. V. Gorshkov, and A. A. Houck, Interacting qubit-photon bound states with superconducting circuits, *Phys. Rev. X* **9**, 011021 (2019).
- [72] P. Lodahl, S. Mahmoodian, S. Stobbe, A. Rauschenbeutel, P. Schneeweiss, J. Volz, H. Pichler, and P. Zoller, Chiral quantum optics, *Nature* **541**, 473 (2017).
- [73] M. Mirhosseini, E. Kim, V. S. Ferreira, M. Kalae, A. Sipahigil, A. J. Keller, and O. Painter, Superconducting metamaterials for waveguide quantum electrodynamics, *Nature communications* **9**, 3706 (2018).
- [74] V. S. Ferreira, J. Banker, A. Sipahigil, M. H. Matheny, A. J. Keller, E. Kim, M. Mirhosseini, and O. Painter, Collapse and revival of an artificial atom coupled to a structured photonic reservoir, *Phys. Rev. X* **11**, 041043 (2021).
- [75] X. Gu, A. F. Kockum, A. Miranowicz, Y.-x. Liu, and F. Nori, Microwave photonics with superconducting quantum circuits, *Physics Reports* **718**, 1 (2017).
- [76] D. Morrone, M. A. Rossi, and M. G. Genoni, Daemonic ergotropy in continuously monitored open quantum batteries, *Phys. Rev. Appl.* **20**, 044073 (2023).
- [77] F. Pirmoradian and K. Mølmer, Aging of a quantum battery, *Phys. Rev. A* **100**, 043833 (2019).
- [78] S. Zakavati, F. T. Tabesh, and S. Salimi, Bounds on charging power of open quantum batteries, *Phys. Rev. E* **104**, 054117 (2021).
- [79] K. Xu, H.-J. Zhu, G.-F. Zhang, and W.-M. Liu, Enhancing the performance of an open quantum battery via environment engineering, *Phys. Rev. E* **104**, 064143 (2021).
- [80] C. Shang and H. Li, Resonance-dominant optomechanical entanglement in open quantum systems, *Phys. Rev. Appl.* **21**, 044048 (2024).
- [81] M. Carrega, A. Crescente, D. Ferraro, and M. Sassetti, Dissipative dynamics of an open quantum battery, *New Journal of Physics* **22**, 083085 (2020).
- [82] Y. Yao and X. Q. Shao, Optimal charging of open spin-chain quantum batteries via homodyne-based feedback control, *Phys. Rev. E* **106**, 014138 (2022).
- [83] F. Barra, Dissipative charging of a quantum battery, *Phys. Rev. Lett.* **122**, 210601 (2019).
- [84] F. Kamin, F. Tabesh, S. Salimi, F. Kheirandish, and A. C. Santos, Non-markovian effects on charging and self-discharging process of quantum batteries, *New Journal of Physics* **22**, 083007 (2020).
- [85] S.-Y. Bai and J.-H. An, Floquet engineering to reactivate a dissipative quantum battery, *Phys. Rev. A* **102**, 060201 (2020).
- [86] W. P. Su, J. R. Schrieffer, and A. J. Heeger, Solitons in polyacetylene, *Phys. Rev. Lett.* **42**, 1698 (1979).
- [87] W. P. Su, J. R. Schrieffer, and A. J. Heeger, Soliton excitations in polyacetylene, *Phys. Rev. B* **22**, 2099 (1980).
- [88] Z. Gong, M. Bello, D. Malz, and F. K. Kunst, Anomalous

- behaviors of quantum emitters in non-hermitian baths, *Phys. Rev. Lett.* **129**, 223601 (2022).
- [89] Z. Gong, M. Bello, D. Malz, and F. K. Kunst, Bound states and photon emission in non-hermitian nanophotonics, *Phys. Rev. A* **106**, 053517 (2022).
- [90] A. González-Tudela and J. I. Cirac, Markovian and non-markovian dynamics of quantum emitters coupled to two-dimensional structured reservoirs, *Phys. Rev. A* **96**, 043811 (2017).
- [91] Z. Gong, S. Higashikawa, and M. Ueda, Zeno hall effect, *Phys. Rev. Lett.* **118**, 200401 (2017).
- [92] R. Alicki, Master equations for a damped nonlinear oscillator and the validity of the markovian approximation, *Phys. Rev. A* **40**, 4077 (1989).
- [93] See supplementary material.
- [94] A. González-Tudela and J. I. Cirac, Quantum emitters in two-dimensional structured reservoirs in the nonperturbative regime, *Phys. Rev. Lett.* **119**, 143602 (2017).
- [95] C. Cohen-Tannoudji, J. Dupont-Roc, and G. Grynberg, *Atom-photon interactions: basic processes and applications* (John Wiley & Sons, 1998).
- [96] G. C. Ménard, S. Guissart, C. Brun, S. Pons, V. S. Stolyarov, F. Debontridder, M. V. Leclerc, E. Janod, L. Cario, D. Roditchev, *et al.*, Coherent long-range magnetic bound states in a superconductor, *Nature Physics* **11**, 1013 (2015).
- [97] J. Q. Quach and W. J. Munro, Using dark states to charge and stabilize open quantum batteries, *Phys. Rev. Appl.* **14**, 024092 (2020).
- [98] L. Leonforte, A. Carollo, and F. Ciccarello, Vacancy-like dressed states in topological waveguide qed, *Phys. Rev. Lett.* **126**, 063601 (2021).
- [99] V. Popkov and C. Presilla, Full spectrum of the liouvillian of open dissipative quantum systems in the zeno limit, *Phys. Rev. Lett.* **126**, 190402 (2021).
- [100] N. Hatano and D. R. Nelson, Localization transitions in non-hermitian quantum mechanics, *Phys. Rev. Lett.* **77**, 570 (1996).
- [101] T. Shi, Y.-H. Wu, A. González-Tudela, and J. I. Cirac, Bound states in boson impurity models, *Phys. Rev. X* **6**, 021027 (2016).
- [102] T. Shi, Y. H. Wu, A. González-Tudela, and J. I. Cirac, Effective many-body hamiltonians of qubit-photon bound states, *New Journal of Physics* **20**, 105005 (2018).
- [103] T. Shi, S. Fan, and C. P. Sun, Two-photon transport in a waveguide coupled to a cavity in a two-level system, *Phys. Rev. A* **84**, 063803 (2011).
- [104] U. Schollwöck, The density-matrix renormalization group in the age of matrix product states, *Annals of physics* **326**, 96 (2011).
- [105] Y. Tanimura, Numerically “exact” approach to open quantum dynamics: The hierarchical equations of motion (heom), *The Journal of chemical physics* **153** (2020).

Supplemental Material for “Topological Quantum Battery”

Zhi-Guang Lu¹, Guoqing Tian, Xin-You Lü^{1,*}, Cheng Shang^{2,3,†}

¹*School of Physics, Huazhong University of Science and Technology, Wuhan, 430074, People’s Republic of China*

²*Department of Physics, The University of Tokyo, 5-1-5 Kashiwanoha, Kashiwa, Chiba 277-8574, Japan*

³*Analytical quantum complexity RIKEN Hakubi Research Team,*

RIKEN Center for Quantum Computing (RQC), 2-1 Hirosawa, Wako, Saitama 351-0198, Japan

This supplement material contains three parts: I. Exact dynamics of a quantum charger and a quantum battery coupled to a structured bosonic environment; II. The dynamics of a quantum battery in a topological environment; III. Quantum battery performance in different configurations. IV. Effects of disorder to the performance of a quantum battery.

S1. EXACT DYNAMICS OF A QUANTUM CHARGER AND A QUANTUM BATTERY COUPLED TO A STRUCTURED BOSONIC ENVIRONMENT

In this section, we present the exact dynamical expression for the charging of a quantum battery (QB) by a quantum charger through an external environment. Firstly, we consider that a quantum battery B and a quantum charger C are concurrently coupled with a structured bosonic bath. The Hamiltonian of the total system under the rotating-wave approximation reads $H_{\text{tot}} = H_{\text{sys}} + H_{\text{bath}} + H_{\text{int}}$, where

$$H_{\text{sys}} = \frac{\omega_e}{2}\sigma_z^B + \frac{\omega_e}{2}\sigma_z^C + \Omega_{12}^{\alpha\beta}(\sigma_+^B\sigma_-^C + \sigma_+^C\sigma_-^B), \quad H_{\text{int}} = g(\sigma_-^B o_{x_1,\alpha}^\dagger + \sigma_+^B o_{x_1,\alpha} + \sigma_-^C o_{x_2,\beta}^\dagger + \sigma_+^C o_{x_2,\beta}), \quad (\text{S1})$$

and $\Omega_{12}^{\alpha\beta} = \Omega\delta_{x_1,x_2}\delta_{\alpha,\beta}$ with $\Omega \in \mathbb{R}$. Here, H_{sys} represents the Hamiltonian of the QB and the quantum charger, and H_{bath} is the Hamiltonian of the structured bosonic bath. The interaction Hamiltonian between the system and the bath is represented by H_{int} , where σ_+^B (σ_+^C) and σ_-^B (σ_-^C) represent the raising and lowering Pauli operators of QB (quantum charger), respectively, while $o_{x_j,\alpha}$ and $o_{x_j,\alpha}^\dagger$ denote the annihilation and creation operators at the position $x_{j,\alpha}$ of bath, respectively. Without loss of generality, we assume that the spectrum of H_{bath} possesses energy band structure. Note that, for consistency with the main text, the second subscript $\alpha \in \{A, B\}$ in $o_{x_j,\alpha}$ is used to emphasize different sublattices, i.e., $o_{x_j,A} \equiv a_j$ and $o_{x_j,B} \equiv b_j$.

To analytically solve the dynamics of the two-level system, we assume that the bath is in the thermodynamic limit in the following derivations. Consequently, the time-evolution operator of the system can be obtained by the Inverse-Fourier transform of the Green’s function [S1]

$$U(t) = e^{-iH_{\text{tot}}t} = \frac{1}{2\pi i} \int_{\mathcal{C}} G_{\text{tot}}(z) e^{-izt} dz = \frac{1}{2\pi i} \int_{\mathcal{C}} \frac{1}{z - H_{\text{tot}}} e^{-izt} dz, \quad (\text{S2})$$

where the integration path \mathcal{C} lies immediately above the real axis in the complex plane, extending infinitely from right to left. In the single-excitation subspace, to explore the dynamics of QB, we need to project the evolution operator $U(t)$ onto the subspace of the system involving QB and quantum charger. Thus, we define

$$P \equiv (|e, g\rangle\langle e, g| + |g, e\rangle\langle g, e|) \otimes |\text{vac}\rangle\langle \text{vac}|, \quad Q \equiv |g, g\rangle\langle g, g| \otimes \sum_{j,\alpha} o_{j,\alpha}^\dagger |\text{vac}\rangle\langle \text{vac}| o_{j,\alpha}, \quad (\text{S3})$$

which satisfy $P + Q = \mathbb{I}_1$, where \mathbb{I}_1 is the identity operator in the single-excitation subspace. For the sake of simplicity, we define $|e_1\rangle \equiv |e, g\rangle$ and $|e_2\rangle \equiv |g, e\rangle$ in the following steps. As a result, the evolution operator projected onto the subspace of the system can be written as

$$PU(t)P = \frac{1}{2\pi i} \int_{\mathcal{C}} PG_{\text{tot}}(z)Pe^{-izt} dz, \quad (\text{S4})$$

where

$$PG_{\text{tot}}(z)P = \frac{P}{z - PH_{\text{sys}}P - P\Sigma(z)P}, \quad P\Sigma(z)P = PH_{\text{int}}P + PH_{\text{int}}\frac{Q}{z - QH_{\text{tot}}Q}H_{\text{int}}P. \quad (\text{S5})$$

Since $PH_{\text{int}}P = QH_{\text{int}}Q = QH_{\text{sys}}Q = 0$, the last term in (S5) can be further simplified as

$$P\Sigma(z)P = PH_{\text{int}}\frac{Q}{z - H_{\text{bath}}}H_{\text{int}}P = PH_{\text{int}}G_{\text{bath}}(z)H_{\text{int}}P, \quad \text{with } G_{\text{bath}}(z) = Q(z - H_{\text{bath}})^{-1}Q. \quad (\text{S6})$$

In the basis $\{|e_1; \text{vac}\rangle, |e_2; \text{vac}\rangle\}$, the first term in (S5) can be written in a matrix form as

$$\begin{bmatrix} G_{11}(z) & G_{12}(z) \\ G_{21}(z) & G_{22}(z) \end{bmatrix} = \begin{bmatrix} z - \omega_e - \Sigma_{11}(z) & -\Omega_{12}^{\alpha\beta} - \Sigma_{12}(z) \\ -\Omega_{12}^{\alpha\beta} - \Sigma_{21}(z) & z - \omega_e - \Sigma_{22}(z) \end{bmatrix}^{-1}, \quad (\text{S7})$$

where

$$G_{mn}(z) = \langle e_m; \text{vac} | PG_{\text{tot}}(z)P | e_n; \text{vac} \rangle, \quad \Sigma_{mn}(z) = \langle e_m; \text{vac} | P\Sigma(z)P | e_n; \text{vac} \rangle. \quad (\text{S8})$$

According to Eq. (S6), by inserting H_{int} into $\Sigma_{mn}(z)$, we have

$$\Sigma_{11}^{\alpha\alpha}(z) = \Sigma_{11}(z) = g^2 \langle \text{vac} | o_{x_{1,\alpha}}(z - H_{\text{bath}})^{-1} o_{x_{1,\alpha}}^\dagger | \text{vac} \rangle \equiv g^2 G(x_{1,\alpha}, x_{1,\alpha}; z), \quad (\text{S9})$$

$$\Sigma_{12}^{\alpha\beta}(z) = \Sigma_{12}(z) = g^2 \langle \text{vac} | o_{x_{1,\alpha}}(z - H_{\text{bath}})^{-1} o_{x_{2,\beta}}^\dagger | \text{vac} \rangle \equiv g^2 G(x_{1,\alpha}, x_{2,\beta}; z), \quad (\text{S10})$$

$$\Sigma_{21}^{\beta\alpha}(z) = \Sigma_{21}(z) = g^2 \langle \text{vac} | o_{x_{2,\beta}}(z - H_{\text{bath}})^{-1} o_{x_{1,\alpha}}^\dagger | \text{vac} \rangle \equiv g^2 G(x_{2,\beta}, x_{1,\alpha}; z), \quad (\text{S11})$$

$$\Sigma_{22}^{\beta\beta}(z) = \Sigma_{22}(z) = g^2 \langle \text{vac} | o_{x_{2,\beta}}(z - H_{\text{bath}})^{-1} o_{x_{2,\beta}}^\dagger | \text{vac} \rangle \equiv g^2 G(x_{2,\beta}, x_{2,\beta}; z), \quad (\text{S12})$$

where $\Sigma_{12}^{\alpha\beta}(z)$ refers to the self-energy of the two-level systems and $G(x_{1,\alpha}, x_{2,\beta}; z)$ represents the single-particle Green's function of the bath. As a result, according to Eq. (S7), the projected evolution operator in Eq. (S4) is given by

$$PU(t)P = \frac{1}{2\pi i} \int_{\mathcal{C}} dz \frac{e^{-izt}}{\mathcal{D}(z)} \begin{bmatrix} |e_1; \text{vac}\rangle \\ |e_2; \text{vac}\rangle \end{bmatrix}^T \begin{bmatrix} z - \omega_e - \Sigma_{22}^{\beta\beta}(z) & \Omega_{12}^{\alpha\beta} + \Sigma_{21}^{\beta\alpha}(z) \\ \Omega_{12}^{\alpha\beta} + \Sigma_{12}^{\alpha\beta}(z) & z - \omega_e - \Sigma_{11}^{\alpha\alpha}(z) \end{bmatrix} \begin{bmatrix} |e_1; \text{vac}\rangle \\ |e_2; \text{vac}\rangle \end{bmatrix}, \quad (\text{S13})$$

where

$$\mathcal{D}(z) = [z - \omega_e - \Sigma_{11}^{\alpha\alpha}(z)][z - \omega_e - \Sigma_{22}^{\beta\beta}(z)] - [\Omega_{12}^{\alpha\beta} + \Sigma_{12}^{\alpha\beta}(z)][\Omega_{12}^{\alpha\beta} + \Sigma_{21}^{\beta\alpha}(z)]. \quad (\text{S14})$$

Finally, let us assume that the total system is prepared in the initial state $|\psi(0)\rangle = |e_1; \text{vac}\rangle$, i.e., the quantum charger is in the excited state, QB is in the ground state, and the environment is in the vacuum state. According to Eq. (S13), the probability amplitude for QB to be in the excited state $|e_2; \text{vac}\rangle$ at t time is given by

$$c_{\text{B}}(t) = \langle e_2; \text{vac} | PU(t)P | e_1; \text{vac} \rangle = \frac{1}{2\pi i} \int_{\mathcal{C}} \frac{\Sigma_{12}^{\alpha\beta} + \Omega_{12}^{\alpha\beta}}{\mathcal{D}(z)} e^{-izt} dz, \quad (\text{S15})$$

and the reduced density matrix of QB is computed as

$$\rho_{\text{B}}(t) = \text{Tr}_{\text{charger} \otimes \text{bath}} [|\psi(t)\rangle\langle\psi(t)|] = |c_{\text{B}}(t)|^2 |e\rangle\langle e| + [1 - |c_{\text{B}}(t)|^2] |g\rangle\langle g|. \quad (\text{S16})$$

S2. THE DYNAMICS OF A QUANTUM BATTERY IN A TOPOLOGICAL ENVIRONMENT

In this section, we show the full derivation of the setup in the main text. We exploring the QB dynamics in a topological environment, both with and without dissipation. We begin with a detailed discussion of the topological environment in subsection A and B. Next, we derive an analytical expressions for self-energy in the dissipative topological environment and demonstrate the connection between bound-state energies and QB dynamics in the long-time limit.

A. Su-Schrieffer-Heeger model without dissipation

Here, we choose the simplest topological model, the Su-Schrieffer-Heeger (SSH) model [S2], as a topological environment. For simplicity, we employ two abbreviations $o_{x_{j,A}} \equiv a_j$ and $o_{x_{j,B}} \equiv b_j$. By setting $\hbar = 1$, the Hamiltonian

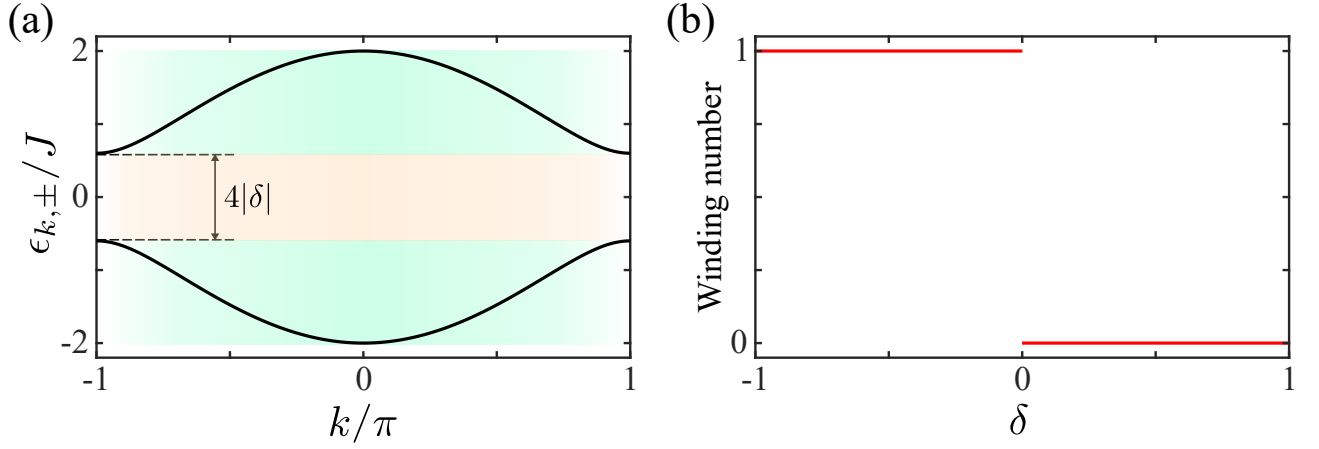


FIG. S1. (a) Dispersion relations $\epsilon_{k,\pm}$ of the Su-Schrieffer-Heeger environment with periodical boundary conditions. The parameter is set as $|\delta| = 0.3$. (b) The winding number as function of the dimerization strength δ . When $\delta < 0$, the model is in a topologically nontrivial phase with a winding number of one. Conversely, when $\delta > 0$, the model is in a topologically trivial phase with a winding number of zero.

of the topological environment is given by

$$H_{\text{bath}} = \sum_{j=1}^N \omega_c (a_j^\dagger a_j + b_j^\dagger b_j) + J_+ \sum_{j=1}^N (a_j^\dagger b_j + b_j^\dagger a_j) + J_- \sum_{j=1}^N (b_j^\dagger a_{j+1} + a_{j+1}^\dagger b_j), \quad (\text{S17})$$

where $a_j (a_j^\dagger)$ and $b_j (b_j^\dagger)$ are the annihilation (creation) operators of boson on the sites a and b at position j , respectively. The resonant frequency of these modes is ω_c . The topological waveguide consists of two interspersed photonic lattices with alternating nearest-neighbor hopping $J_\pm = J(1 \pm \delta)$ between bosonic modes. Here, J defines the hopping strength, and δ , known as the dimerization parameter, controls the asymmetry between the lattices. Under the periodic boundary conditions (i.e., $a_{N+j} = a_j$ and $b_{N+j} = b_j$) and in the momentum space with

$$a_k^\dagger = \frac{1}{\sqrt{N}} \sum_{j=1}^N e^{ikj} a_j^\dagger, \quad b_k^\dagger = \frac{1}{\sqrt{N}} \sum_{j=1}^N e^{ikj} b_j^\dagger, \quad k = \frac{2\pi}{N}n, \quad n \in (-N/2, N/2], \quad (\text{S18})$$

the environment Hamiltonian in the momentum space can be written as $H_{\text{bath}} = \sum_k \mathbf{o}_k^\dagger \mathbf{h}_k \mathbf{o}_k$, with $\mathbf{o}_k = [a_k, b_k]^T$, and the corresponding Bloch Hamiltonian reads

$$\mathbf{h}_k = \begin{bmatrix} \omega_c & f_k \\ f_k^* & \omega_c \end{bmatrix} = \text{Re}[f_k] \sigma_x - \text{Im}[f_k] \sigma_y + \omega_c \sigma_0, \quad (\text{S19})$$

where $f_k = J(1 + \delta) + J(1 - \delta)e^{-ik} \equiv \omega_k e^{i\phi_k}$ (with $\omega_k > 0$) is the coupling coefficient in the momentum space between the bosonic modes of a_k and b_k . Hereafter we set ω_c as the energy reference. By simply diagonalizing \mathbf{h}_k , the Hamiltonian H_{bath} in Eq. (S17) can be further written as

$$H_{\text{bath}} = \sum_k \begin{bmatrix} u_k^\dagger & l_k^\dagger \end{bmatrix} \begin{bmatrix} \omega_k & 0 \\ 0 & -\omega_k \end{bmatrix} \begin{bmatrix} u_k \\ l_k \end{bmatrix} = \sum_k [\omega_k u_k^\dagger u_k - \omega_k l_k^\dagger l_k], \quad (\text{S20})$$

where $u_k/l_k = (\pm a_k + b_k e^{i\phi_k})/\sqrt{2}$, $\omega_k = J\sqrt{2(1 + \delta^2) + 2(1 - \delta^2)\cos(k)}$, and $\phi_k = \arctan[\text{Im}(f_k)/\text{Re}(f_k)]$. The corresponding dispersion relations are given by $\epsilon_{k,\pm} = \pm\omega_k$, where the subscript $+$ ($-$) denotes the upper (lower) energy band of the SSH environment.

In Fig.S1(a), we present the dispersion relation for a dimerization parameter $|\delta| = 0.3$. The energy bands of the bath are observed to be symmetric with respect to the cavity resonant frequency ω_c . The energy bands span the range $[-2J, -2|\delta|J] \cup [2|\delta|J, 2J]$, featuring a central bandgap of $4|\delta|J$. These energy bands can be adjusted by varying the dimerization strength δ . In the SSH model, the topological properties of the system are characterized by the winding number, which takes values of either one or zero, depending on the parameters of the system. In Fig.S1(b), we depict

the winding number of the SSH bath. In the case in which the intracell hopping strength outweighs the intercell hopping strength (i.e., $\delta > 0$), the winding number equals to zero, corresponding to the so-called topologically trivial phase. Conversely, when the intercell hopping strength dominates over the intracell hopping strength (i.e., $\delta < 0$), the winding number is one, indicating a topologically nontrivial phase.

B. Su-Schrieffer-Heeger model with dissipation

Let us consider a realistic scenario: a one-dimensional SSH photonic lattice with engineered photon loss [S3]. Under the Born-Markov and rotating-wave approximations, the equation of motion reads

$$\dot{\rho}_t = -i[H_{\text{sys}} + H_{\text{bath}} + H_{\text{int}}, \rho_t] + \mathcal{L}_a \rho_t + \mathcal{L}_b \rho_t, \quad (\text{S21})$$

where H_{sys} , H_{int} , and H_{bath} are defined by Eqs. (S1) and (S17). The photon dissipators for the different sublattices are given by $\mathcal{L}_a = \kappa_a \sum_j \mathcal{D}[a_j]$ and $\mathcal{L}_b = \kappa_b \sum_j \mathcal{D}[b_j]$, where κ_a (κ_b) controls the photon loss rates of sublattice A (B), and $\mathcal{D}[L]\rho \equiv L\rho L^\dagger - \{L^\dagger L, \rho\}/2$ is the Lindblad superoperator. To find the solution to Eq. (S21) in the single-excitation sector, we rewrite the Lindblad master equation (S21) as

$$\dot{\rho}_t = -i(H_{\text{eff}}\rho_t - \rho_t H_{\text{eff}}^\dagger) + \kappa_a \sum_{j=1}^N a_j \rho_t a_j^\dagger + \kappa_b \sum_{j=1}^N b_j \rho_t b_j^\dagger, \quad (\text{S22})$$

where a_j and b_j within the last two terms on the right-hand side (RHS) of Eq. (S22) are the ‘‘jump’’ operators associated with the sublattices dissipation resulting from emission into free space, and H_{eff} is the effective non-Hermitian (NH) Hamiltonian for the dissipative system, i.e., $H_{\text{eff}} = H_{\text{sys}} + H_{\text{bath}}^{\text{eff}} + H_{\text{int}}$ with $H_{\text{bath}}^{\text{eff}} = H_{\text{bath}} - (i/2) \sum_j (\kappa_a a_j^\dagger a_j + \kappa_b b_j^\dagger b_j)$. In this form, the terms $\kappa_a \sum_j a_j \rho_t a_j^\dagger$ and $\kappa_b \sum_j b_j \rho_t b_j^\dagger$ are often called the recycling terms, as it recycles the population that is lost from certain states due to the effective NH Hamiltonian, placing it in other states. For the initial state $|\psi(0)\rangle$ in the single-excitation subspace, on the one hand, the time evolution under the effective NH Hamiltonian is given by $|\psi(t)\rangle = \exp(-iH_{\text{eff}}t)|\psi(0)\rangle$, resulting in a non-normalized final state with a norm squared that monotonically decreases over time, as shown by the blue line in Fig. S2(a). On the other hand, once the recycling terms work, i.e., when a jump process occurs, the final state deterministically transitions to the zero-excitation state $|g, g; \text{vac}\rangle$. According to quantum trajectory method [S4], whether a jump process occurs at time t is determined by comparing a random number δ_t between 0 and 1 with the norm squared $\langle\psi(t)|\psi(t)\rangle = \|\exp(-iH_{\text{eff}}t)|\psi(0)\rangle\|^2$. Specifically, if $\delta_t > \langle\psi(t)|\psi(t)\rangle$, the jump occurs; otherwise, it does not, as illustrated by the red and yellow regions in Fig. S2(a).

Then, we focus on the state at time t and generate N random numbers uniformly distributed between 0 and 1. For the sake of simplicity, we define N_1 and N_2 as the counts of no-jump and jump occurrences, respectively, where $N_1 + N_2 = N$ is satisfied. As a result, based on the condition for the occurrence of jumps, the solution to Eq. (S21) reads

$$\rho_t = \lim_{N \rightarrow \infty} \frac{|\tilde{\psi}(t)\rangle\langle\tilde{\psi}(t)| \times N_1 + |g, g; \text{vac}\rangle\langle g, g; \text{vac}| \times N_2}{N}, \quad (\text{S23})$$

where $|\tilde{\psi}(t)\rangle = |\psi(t)\rangle / \sqrt{\langle\psi(t)|\psi(t)\rangle}$ representing the normalized state. Provided our random number generators are well behaved, these two ratios satisfy

$$\lim_{N \rightarrow \infty} \frac{N_1}{N} = \langle\psi(t)|\psi(t)\rangle, \quad \lim_{N \rightarrow \infty} \frac{N_2}{N} = 1 - \lim_{N \rightarrow \infty} \frac{N_1}{N} = 1 - \langle\psi(t)|\psi(t)\rangle = p_t. \quad (\text{S24})$$

Finally, by plugging Eq. (S24) into Eq. (S23), we have

$$\rho_t = |\psi(t)\rangle\langle\psi(t)| + p_t |g, g; \text{vac}\rangle\langle g, g; \text{vac}| = e^{-iH_{\text{eff}}t} \rho_0 e^{iH_{\text{eff}}^\dagger t} + p_t |g, g; \text{vac}\rangle\langle g, g; \text{vac}|. \quad (\text{S25})$$

If the initial state is a mixed state ρ_0 , the norm squared $\langle\psi(t)|\psi(t)\rangle$ mentioned above should be rewritten as $\text{Tr}[e^{-iH_{\text{eff}}t} \rho_0 e^{iH_{\text{eff}}^\dagger t}]$. Notice that $\text{Tr}[e^{-iH_{\text{eff}}t} \rho_0 e^{iH_{\text{eff}}^\dagger t}] = \langle\psi(t)|\psi(t)\rangle$ when $\rho_0 = |\psi(0)\rangle\langle\psi(0)|$. In fact, when we replace the total Hamiltonian H_{tot} in Eq. (S2) with the effective NH Hamiltonian H_{eff} , i.e., $H_{\text{bath}} \rightarrow H_{\text{bath}}^{\text{eff}}$, the derivation procedures from Eq. (S2) to Eq. (S16) remain valid.

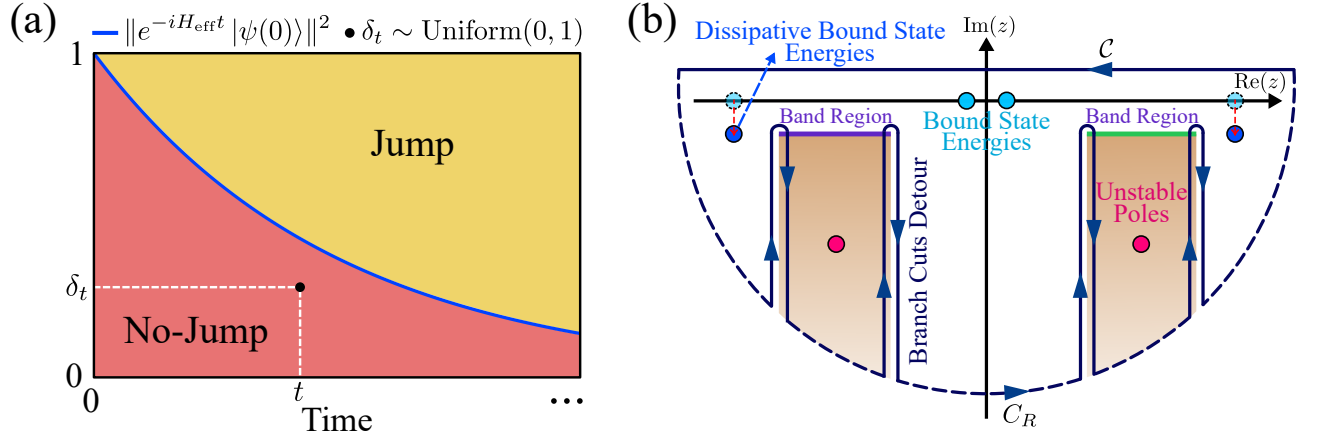


FIG. S2. (a) The norm squared of the evolved state governed by the effective NH Hamiltonian H_{eff} as a function of time. For a single trajectory, the occurrence of a quantum jump at time t can be determined by comparing a random number δ_t with the norm squared at that time, as indicated by the black dot falling within the red region. (b) An integration contour (horizontal dark blue line) to calculate Eq. (S15). One needs to close the contour of integration in the lower half of the complex plane (dashed and vertical dark blue line) to evaluate the integration. Here, the information including (dissipative) bound-state energies, branch cuts detour, unstable poles, and band regions, within the lower half of the complex plane is given by the effective NH Hamiltonian described by Sec. S2B. At the band edges the path changes from the first to the second Riemann sheet of the integrand $\mathcal{C}(z)$ (brown areas).

Therefore, we only focus on studying the effective NH Hamiltonian when we restrict ourselves to the single-excitation subspace. Following Eqs. (S17-S20), we express the corresponding NH Bloch Hamiltonian as

$$\tilde{\mathbf{h}}_k = \begin{bmatrix} -i\kappa_a/2 & f_k \\ f_k^* & -i\kappa_b/2 \end{bmatrix} = \text{Re}[f_k]\sigma_x - \text{Im}[f_k]\sigma_y - i\kappa_- \sigma_z - i\kappa_+ \sigma_0, \quad (\text{S26})$$

whose energy dispersion reads $\tilde{\epsilon}_{k,\pm} = -i\kappa_{\pm} \pm \tilde{\omega}_k$, where $\tilde{\omega}_k = \sqrt{\omega_k^2 - \kappa_-^2}$ and $\kappa_{\pm} = (\kappa_a \pm \kappa_b)/4$. Remarkably, we find that the system exhibits a passive parity-time symmetry [S5]

$$\sigma_x (\tilde{\mathbf{h}}_k + i\kappa_+ \sigma_0)^* \sigma_x = \tilde{\mathbf{h}}_k + i\kappa_+ \sigma_0 \quad (\text{S27})$$

and has two exceptional points (EPs) at $k_{\text{EP}} = \pm \arccos[(\kappa_-^2 - 2J^2(1 + \delta^2))/(2J^2(1 - \delta^2))]$ in the Brillouin zone for $|\delta| \leq |\kappa_-/(2J)| < 1$. Then, by diagonalizing $\tilde{\mathbf{h}}_k$, the effective NH Hamiltonian $H_{\text{bath}}^{\text{eff}}$ in Eq. (S22) can be further written as

$$H_{\text{bath}}^{\text{eff}} = \sum_k \begin{bmatrix} u_{k,L}^\dagger & l_{k,L}^\dagger \end{bmatrix} \begin{bmatrix} \tilde{\epsilon}_{k,+} & 0 \\ 0 & \tilde{\epsilon}_{k,-} \end{bmatrix} \begin{bmatrix} u_{k,R} \\ l_{k,R} \end{bmatrix} = \sum_k [\tilde{\epsilon}_{k,+} u_{k,L}^\dagger u_{k,R} + \tilde{\epsilon}_{k,-} l_{k,L}^\dagger l_{k,R}] \quad (\text{S28})$$

with

$$u_{k,L}^\dagger/l_{k,L}^\dagger = \frac{1}{\sqrt{2}} \left[\pm a_k^\dagger + \frac{\tilde{\omega}_k \pm i\kappa_-}{\omega_k e^{i\phi_k}} b_k \right], \quad u_{k,R}/l_{k,R} = \frac{1}{\sqrt{2}} \left[\frac{\pm \tilde{\omega}_k - i\kappa_-}{\tilde{\omega}_k} a_k + \frac{\omega_k e^{i\phi_k}}{\tilde{\omega}_k} b_k \right], \quad (\text{S29})$$

which satisfy $u_{k,R} = u_{k,L} = u_k$, $l_{k,R} = l_{k,L} = l_k$, and $\tilde{\epsilon}_{k,\pm} = \epsilon_{k,\pm}$ when $\kappa_a = \kappa_b = 0$.

C. The calculation of self-energy in the dissipative topological environment

To evaluate the integral (S15), these expressions (S9)-(S12), referred to as the self-energies of two quantum emitters, require further computation. When $\kappa_a = \kappa_b = 0$, the dissipative environment degenerates into a non-dissipative environment. For the sake of generality, we compute the self-energy directly within the dissipative topological environment.

Firstly, we transform Q in Eq. (S3) into momentum space, i.e.,

$$Q = |g, g\rangle\langle g, g| \otimes \sum_j (a_j^\dagger |\text{vac}\rangle\langle \text{vac}| a_j + b_j^\dagger |\text{vac}\rangle\langle \text{vac}| b_j) = |g, g\rangle\langle g, g| \otimes \sum_k (|u_{k,L}\rangle\langle u_{k,R}| + |l_{k,L}\rangle\langle l_{k,R}|), \quad (\text{S30})$$

where $|u_{k,L}(l_{k,L})\rangle = u_{k,L}^\dagger(l_{k,L}^\dagger) |\text{vac}\rangle$ and $\langle u_{k,R}(l_{k,R})| = \langle \text{vac}| u_{k,R}(l_{k,R})$, which satisfy $\langle u_{k,R}|u_{k',L}\rangle = \langle l_{k,R}|l_{k',L}\rangle = \delta_{k,k'}$ and $\langle u_{k,R}|l_{k',L}\rangle = \langle l_{k,R}|u_{k',L}\rangle = 0$. For the sake of simplicity, we define $\tilde{Q} = \sum_k (|u_{k,L}\rangle\langle u_{k,R}| + |l_{k,L}\rangle\langle l_{k,R}|)$. According to Eqs. (S10), (S18), (S28), and (S30), we have

$$\begin{aligned} G(x_{1,\alpha}, x_{2,\beta}; z) &= \langle \text{vac}| o_{x_{1,\alpha}} (z - H_{\text{bath}}^{\text{eff}})^{-1} o_{x_{2,\beta}}^\dagger |\text{vac}\rangle = \langle \text{vac}| o_{x_{1,\alpha}} \tilde{Q} (z - H_{\text{bath}}^{\text{eff}})^{-1} \tilde{Q} o_{x_{2,\beta}}^\dagger |\text{vac}\rangle \\ &= \langle \text{vac}| o_{x_{1,\alpha}} \sum_k \left[\frac{|u_{k,L}\rangle\langle u_{k,R}|}{z + i\kappa_+ - \tilde{\omega}_k} + \frac{|l_{k,L}\rangle\langle l_{k,R}|}{z + i\kappa_+ + \tilde{\omega}_k} \right] o_{x_{2,\beta}}^\dagger |\text{vac}\rangle. \end{aligned} \quad (\text{S31})$$

For $\alpha = \beta = A$, according to Eq. (S29), Eq. (S31) can be further written as

$$\begin{aligned} G(x_{1,A}, x_{2,A}; z) &= \frac{1}{N} \sum_{k,k',k''} e^{ik'x_1 - ik''x_2} \langle \text{vac}| a_{k'} \left[\frac{|u_{k,L}\rangle\langle u_{k,R}|}{z + i\kappa_+ - \tilde{\omega}_k} + \frac{|l_{k,L}\rangle\langle l_{k,R}|}{z + i\kappa_+ + \tilde{\omega}_k} \right] a_{k''}^\dagger |\text{vac}\rangle \\ &= \frac{1}{2N} \sum_{k,k',k''} e^{ik'x_1 - ik''x_2} \left[\frac{\tilde{\omega}_{k''} - i\kappa_-}{z + i\kappa_+ - \tilde{\omega}_k} + \frac{\tilde{\omega}_{k''} + i\kappa_-}{z + i\kappa_+ + \tilde{\omega}_k} \right] \frac{\delta_{k,k'} \delta_{k,k''}}{\tilde{\omega}_{k''}} \\ &= \frac{1}{N} \sum_k \frac{(z + i\kappa_b/2) e^{ik(x_1 - x_2)}}{z_{\text{nh}}^2 - \omega_k^2} = \int_{-\pi}^{\pi} \frac{dk}{2\pi} \frac{(z + i\kappa_b/2) e^{ikd}}{z_{\text{nh}}^2 - \omega_k^2}, \end{aligned} \quad (\text{S32})$$

where $z_{\text{nh}}^2 = (z + i\kappa_+)^2 + \kappa_-^2$ and $d = x_1 - x_2$. Similarly, for $\alpha = \beta = B$, we have

$$G(x_{1,B}, x_{2,B}; z) = \frac{1}{N} \sum_k \frac{(z + i\kappa_a/2) e^{ikd}}{z_{\text{nh}}^2 - \omega_k^2} = \int_{-\pi}^{\pi} \frac{dk}{2\pi} \frac{(z + i\kappa_a/2) e^{ikd}}{z_{\text{nh}}^2 - \omega_k^2}, \quad (\text{S33})$$

whereas for other cases of α and β , we have

$$G(x_{1,A}, x_{2,B}; z) = \int_{-\pi}^{\pi} \frac{dk}{2\pi} \frac{\omega_k e^{ikd + i\phi_k}}{z_{\text{nh}}^2 - \omega_k^2}, \quad G(x_{1,B}, x_{2,A}; z) = \int_{-\pi}^{\pi} \frac{dk}{2\pi} \frac{\omega_k e^{ikd - i\phi_k}}{z_{\text{nh}}^2 - \omega_k^2}. \quad (\text{S34})$$

By substituting the given dispersion relation, these two integrals in Eqs. (S32) and (S33) can be evaluated as

$$\begin{aligned} G(x_{1,A}, x_{2,A}; z) &= \int_{-\pi}^{\pi} \frac{dk}{2\pi} \frac{(z + i\kappa_b/2) e^{ikd}}{z_{\text{nh}}^2 - J^2[2(1 + \delta^2) + 2(1 - \delta^2) \cos(k)]} = \oint_{|y|=1} \frac{dy}{2\pi i} \frac{(z + i\kappa_b/2) y^d}{J^2(\delta^2 - 1)(y^2 + 1) + [z_{\text{nh}}^2 - 2J^2(1 + \delta^2)]y} \\ &= -\frac{(z + i\kappa_b/2) \sum_{p=\pm} p \tilde{y}_p^{|d|} \Theta[p(1 - |\tilde{y}_+|)]}{\sqrt{z_{\text{nh}}^4 - 4J^2 z_{\text{nh}}^2(1 + \delta^2) + 16J^4 \delta^2}} = G(x_{2,A}, x_{1,A}; z), \end{aligned} \quad (\text{S35})$$

$$\begin{aligned} G(x_{1,B}, x_{2,B}; z) &= \int_{-\pi}^{\pi} \frac{dk}{2\pi} \frac{(z + i\kappa_a/2) e^{ikd}}{z_{\text{nh}}^2 - J^2[2(1 + \delta^2) + 2(1 - \delta^2) \cos(k)]} = \oint_{|y|=1} \frac{dy}{2\pi i} \frac{(z + i\kappa_a/2) y^d}{J^2(\delta^2 - 1)(y^2 + 1) + [z_{\text{nh}}^2 - 2J^2(1 + \delta^2)]y} \\ &= -\frac{(z + i\kappa_a/2) \sum_{p=\pm} p \tilde{y}_p^{|d|} \Theta[p(1 - |\tilde{y}_+|)]}{\sqrt{z_{\text{nh}}^4 - 4J^2 z_{\text{nh}}^2(1 + \delta^2) + 16J^4 \delta^2}} = G(x_{2,B}, x_{1,B}; z), \end{aligned} \quad (\text{S36})$$

where

$$\tilde{y}_{\pm} = \frac{z_{\text{nh}}^2 - 2J^2(1 + \delta^2) \pm \sqrt{z_{\text{nh}}^4 - 4J^2 z_{\text{nh}}^2(1 + \delta^2) + 16J^4 \delta^2}}{2J^2(1 - \delta^2)}, \quad \Theta[x] = \begin{cases} 1 & x \geq 0 \\ 0 & x < 0 \end{cases}. \quad (\text{S37})$$

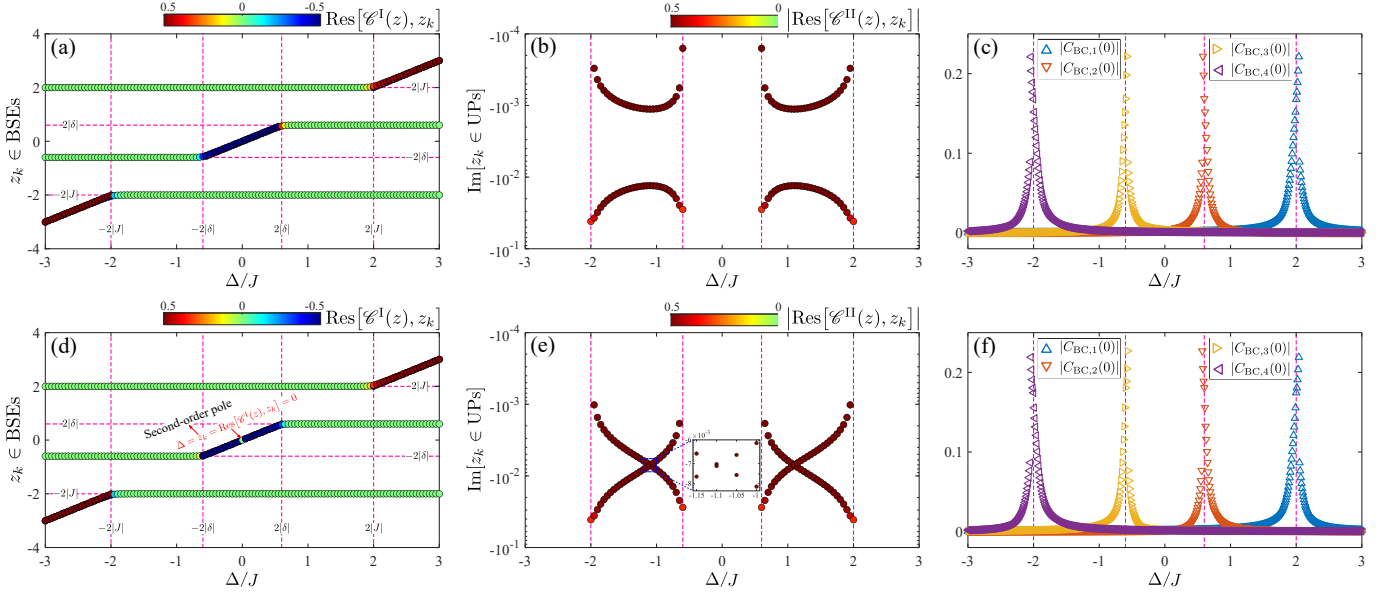


FIG. S3. First row (a)-(c): topologically nontrivial phase ($\delta = -0.3$). Second row (d)-(f): topologically trivial phase ($\delta = 0.3$). Panels (a) and (d) describe the bound-state energies z_k and its corresponding residue $\text{Res}[\mathcal{C}^I(z), z_k]$ as a function of the emitter detuning Δ . Panels (b) and (e) describe the imaginary part of the unstable poles $\text{Im}[z_k]$ and the absolute value of its corresponding residue $|\text{Res}[\mathcal{C}^{II}(z), z_k]|$ as a function of the emitter detuning Δ . Panels (c) and (f) describe the contributions at time $t = 0$ of the branch cut detours $C_{\text{BC},k}(0)$ as a function of the emitter detuning Δ . The system parameters are $g/J = 0.1$, $\alpha = B$, $\beta = A$, and $d = x_1 - x_2 = -1$.

Given $f_k = \omega_k e^{i\phi_k}$ and $f_k^* = \omega_k e^{-i\phi_k}$, these two integrals in Eq. (S34) are evaluated as

$$\begin{aligned}
 G(x_{1,A}, x_{2,B}; z) &= \int_{-\pi}^{\pi} \frac{dk}{2\pi} \frac{J[1 + \delta + (1 - \delta)e^{-ik}]e^{ikd}}{z_{\text{nh}}^2 - J^2[2(1 + \delta^2) + 2(1 - \delta^2)\cos(k)]} = \oint_{|y|=1} \frac{dy}{2\pi i} \frac{J[(1 + \delta)y^d + (1 - \delta)y^{d-1}]}{z_{\text{nh}}^2 - J^2[2(1 + \delta^2) + 2(1 - \delta^2)\cos(k)]} \\
 &= -\frac{J \sum_{p=\pm} p F_d(\tilde{y}_p, \delta) \Theta[p(1 - |\tilde{y}_+|)]}{\sqrt{z_{\text{nh}}^4 - 4J^2 z_{\text{nh}}^2 (1 + \delta^2) + 16J^4 \delta^2}} = G(x_{2,B}, x_{1,A}; z), \tag{S38}
 \end{aligned}$$

$$\begin{aligned}
 G(x_{1,B}, x_{2,A}; z) &= \int_{-\pi}^{\pi} \frac{dk}{2\pi} \frac{J[1 + \delta + (1 - \delta)e^{ik}]e^{ikd}}{z_{\text{nh}}^2 - J^2[2(1 + \delta^2) + 2(1 - \delta^2)\cos(k)]} = \oint_{|y|=1} \frac{dy}{2\pi i} \frac{J[(1 + \delta)y^d + (1 - \delta)y^{d+1}]}{z_{\text{nh}}^2 - J^2[2(1 + \delta^2) + 2(1 - \delta^2)\cos(k)]} \\
 &= -\frac{J \sum_{p=\pm} p F_{d+1}(\tilde{y}_p, -\delta) \Theta[p(1 - |\tilde{y}_+|)]}{\sqrt{z_{\text{nh}}^4 - 4J^2 z_{\text{nh}}^2 (1 + \delta^2) + 16J^4 \delta^2}} = G(x_{2,A}, x_{1,B}; z), \tag{S39}
 \end{aligned}$$

where $F_d(\tilde{y}_p, \delta) = (1 + \delta)\tilde{y}_p^{|d|} + (1 - \delta)\tilde{y}_p^{|d-1|}$.

D. The calculation of probability amplitude for quantum battery

To further obtain the QB dynamics, i.e., calculating the integral in Eq. (S15), we employ residue integration by closing the contour in the lower half of the complex plane, as illustrated in Fig. S2(b). Since the presence of sublattices dissipation makes the distribution of band regions (namely branch cuts) in the complex plane exceedingly intricate in certain cases, the following calculations will focus solely on the non-dissipative SSH environment (see Sec. S2 A). Accordingly, Fig. S2(b) should be slightly modified for the non-dissipative environment as follows: (i) Dissipative bound-state energies should be replaced by bound-state energies; (ii) The band regions should be shifted to the real axis, $\text{Re}[z]$.

Now, let us focus on the integral in Eq. (S15) and its integrand. Since the integrand has branch cuts in the real axis along the regions (i.e., $z \in [-2J, -2|\delta|] \cup [2|\delta|, 2J]$), where the bands of the topological environment are defined (the continuous spectrum of H_{tot}), it is necessary to detour at the band edges to other Riemann sheets of the integrand, as shown in the modified Fig. S2(b). For convenience, we use the symbol $\mathcal{C}(z)$ to represent the integrand excluding

the term $\exp(-izt)$. The analytical expressions for the self-energies presented in Eqs.(S35), (S36), (S38), and (S39) correspond to the integrand in the first Riemann sheet $\mathcal{C}^I(z)$. We can analytically continue it to the second Riemann sheet $\mathcal{C}^{II}(z)$ (brown areas) by simply replacing $\Theta[p(\dots)]$ with $\Theta[-p(\dots)]$ in the expressions of the self-energies. As a result, the integrand in the first and second Riemann sheets is given by

$$\mathcal{C}^{I/II}(z) = \frac{g^2 G^{I/II}(x_{1,\alpha}, x_{2,\beta}; z) + \Omega_{12}^{\alpha\beta}}{\mathcal{D}^{I/II}(z)} \quad (\text{S40})$$

with

$$G^{I/II}(x_{1,A}, x_{2,A}; z) = -\frac{z \sum_{p=\pm} p y_p^{|x_1-x_2|} \Theta[\pm p(1-|y_+|)]}{\sqrt{z^4 - 4J^2 z^2(1+\delta^2) + 16J^4 \delta^2}} = G^{I/II}(x_{1,B}, x_{2,B}; z), \quad (\text{S41})$$

$$G^{I/II}(x_{1,A}, x_{2,B}; z) = -\frac{J \sum_{p=\pm} p F_{x_1-x_2}(y_p, \delta) \Theta[\pm p(1-|y_+|)]}{\sqrt{z^4 - 4J^2 z^2(1+\delta^2) + 16J^4 \delta^2}}, \quad (\text{S42})$$

where $y_{\pm} = \tilde{y}_{\pm}|_{z_{\text{nh}} \rightarrow z}$ representing non-dissipative environment. Here, since $\Sigma_{11}^{\alpha\alpha}(z) = \Sigma_{11}^{\beta\beta}(z)$ and $\Sigma_{12}^{\alpha\beta}(z) = \Sigma_{21}^{\beta\alpha}(z)$, the denominator in Eq. (S40) can be further simplified as

$$\mathcal{D}^{I/II}(z) = [z - \Delta - g^2 G^{I/II}(x_{1,\alpha}, x_{1,\alpha}; z)]^2 - [\Omega_{12}^{\alpha\beta} + g^2 G^{I/II}(x_{1,\alpha}, x_{2,\beta}; z)]^2, \quad (\text{S43})$$

where $\Delta = \omega_e - \omega_c$ is the emitter detuning. On the one hand, since the imaginary part of $\mathcal{C}^I(z + i0^+)$ and $\mathcal{C}^{II}(z - i0^+)$ is nonzero in the band regions, we should only take into account the real poles (i.e., the roots of $\mathcal{D}^I(z) = 0$) of $\mathcal{C}^I(z)$ outside the band regions, corresponding to the bound-state energies (BSEs), and the complex poles (i.e., the roots of $\mathcal{D}^{II}(z) = 0$) of $\mathcal{C}^{II}(z)$ with real part inside band regions, corresponding to the unstable poles (UPs). On the other hand, aside from the integral path \mathcal{C} (which corresponds to Eq. (S15)) and the semicircular path C_R (which vanished as the radius of the semicircle approaches infinity, according to Jordan's lemma), we need to add eight additional integral paths parallel to the imaginary axis, corresponding to the branch cut detours (BCDs), so that these paths form a closed loop on the complex plane, as shown in the modified Fig. S2(b). According to the residue theorem, the sum of the integrals along these paths should equal the sum of the residues at the aforementioned poles. Thus, we have [S6]

$$c_B(t) = \sum_{z_k \in \text{BSEs}} \text{Res}[\mathcal{C}^I(z), z_k] e^{-iz_k t} + \sum_{z_k \in \text{UPs}} \text{Res}[\mathcal{C}^{II}(z), z_k] e^{-iz_k t} - \sum_{k=1}^4 C_{\text{BC},k}(t). \quad (\text{S44})$$

The last term on the RHS in Eq. (S44) represents the contributions of BCDs, which can be computed as

$$C_{\text{BC},k}(t) = (-1)^k \int_0^{\infty} \frac{dy}{2\pi} [\mathcal{D}^I(c_k - iy) - \mathcal{D}^{II}(c_k - iy)] e^{-ic_k t - yt}, \quad (\text{S45})$$

where $c_1 = 2J, c_2 = 2|\delta|, c_3 = -2|\delta|$, and $c_4 = -2J$. Based on the form of Eq. (S44), we note that the QB dynamics is fully described by the contributions from BSEs, UPs, and BCDs. Given that the integrand in Eq. (S45) contains $\exp(-yt)$ with $y \geq 0$, the contribution from BCDs evidently diminishes as time increases. Furthermore, because the imaginary parts of the UPs are negative, their contribution also decay over time. Therefore, only the bound state contributions survive in the long-time limit $t \gg 1/g$, i.e.,

$$c_B(\infty) \equiv \lim_{t \gg 1/g} c_B(t) = \sum_{z_k \in \text{BSEs}} \text{Res}[\mathcal{C}^I(z), z_k] e^{-iz_k t}. \quad (\text{S46})$$

Next, we demonstrate how the residues of the bound-state energies, the absolute values of the residues of the unstable pole, and branch-cut contributions vary with the emitter detuning Δ in both topologically trivial and non-trivial phases. First, as shown in Figs. S3(a) and S3(d), for topologically trivial and non-trivial phases, the number of bound states and the corresponding residues varies with detuning in the same way, except at zero detuning. Particularly at zero detuning, in the topologically non-trivial phase, the two non-zero bound-state energies (their residues are close to ± 0.5 , respectively), which are opposite in sign, will merge into a degenerate zero-energy bound state (its residue approaches to zero). Moreover, the contribution of BSEs becomes most significant only when the detuning falls within the bandgap, and the number of bound states also increases by one compared to those within the bands, except at $\Delta = 0$ in the topologically trivial phase. Second, as shown in Figs. S3(b) and S3(e), UPs appear in pairs only when the detuning is within the bands, and the effective dissipation (i.e., $-\text{Im}[z_k]$) is significantly enhanced in the topologically trivial phase compared to the topologically non-trivial phase. Finally, as shown in Figs. S3(c) and S3(f), the contribution from BCDs at time $t = 0$ is almost identical in both topologically trivial and non-trivial phases and is most significant only when the detuning is near the band edges.

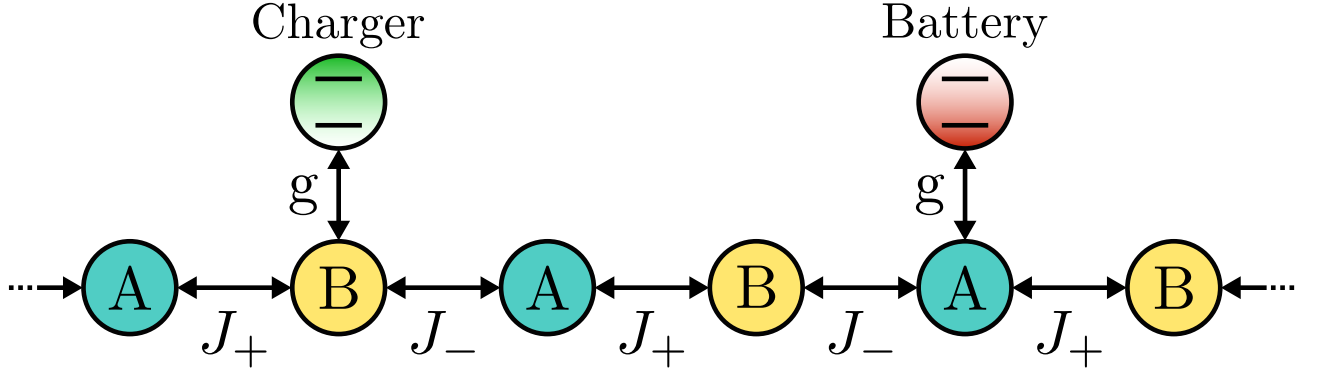


FIG. S4. Configuration-I: The quantum charger and the QB are located in different sublattices, i.e., $x_{1,\alpha} = x_{1,B}$ and $x_{2,\beta} = x_{2,A}$, which indicates that the quantum charger and the QB are not directly coupled, i.e., $\Omega_{12}^{\alpha\beta} = 0$.

S3. QUANTUM BATTERY PERFORMANCE IN DIFFERENT CONFIGURATIONS

To support the phase boundaries outlined in Eq.(10) and the maximum stored energy described in Eq.(11) of the main text, we provide detailed derivations and discussions in the following subsections: subsection A covers the phase diagram of QB, subsection B addresses the dissipation immunity of QB, and subsection C demonstrates how environmental dissipation can be utilized to enhance QB performance over a short time.

A. Phase diagram of quantum battery

Here, the definition of the stored energy for QB is given by $\mathcal{E}(t) = \text{Tr}[\rho_B(t)H_B]$, where $H_B = \omega_e \sigma_+^B \sigma_-^B$ and $\rho_B(t)$ are the free Hamiltonian and the reduced density matrix of QB, respectively. For a general system described in Sec. S1, the reduced density matrix of QB can be obtained from the steps of Eqs. (S2-S16). Then, by substituting Eq. (S16) into $\mathcal{E}(t)$, the stored energy of QB is simplified to $\mathcal{E}(t) = \omega_e |c_B(t)|^2$. The calculation of stored energy of QB is thus reduced to calculating the probability amplitude. According to Eq. (S46), we know that in the long-time limit, only the bound states contribute to the probability amplitude. Therefore, to obtain the maximum stored energy $\max_t[\mathcal{E}(\infty)]$, we need to find the poles of the integrand in Eq. (S15) in band-gap region (i.e., BSEs) by solving the poles equation

$$\mathcal{D}(E_i) = [E_i - \Delta - \Sigma_{11}^{\alpha\alpha}(E_i)][E_i - \Delta - \Sigma_{22}^{\beta\beta}(E_i)] - [\Omega_{12}^{\alpha\beta} + \Sigma_{12}^{\alpha\beta}(E_i)][\Omega_{12}^{\beta\alpha} + \Sigma_{21}^{\beta\alpha}(E_i)] = 0. \quad (\text{S47})$$

Subsequently, we focus solely on the system presented in Fig.2(a-d) of the main text, as depicted in Fig.(S4). The corresponding total Hamiltonian is denoted as

$$H_{\text{tot}} = \frac{\omega_e}{2} \sigma_z^B + \frac{\omega_e}{2} \sigma_z^C + H_{\text{bath}} + g(\sigma_+^B o_{x_{1,B}} + \sigma_+^C o_{x_{2,A}} + \text{H.c.}), \quad (\text{S48})$$

where H_{bath} is given by Eq. (S17). For simplicity, we assume that the quantum charger is always positioned on the left side of the QB, which implies $d = x_1 - x_2 \in \mathbb{Z}^-$. According to these expressions of the self-energies in Eqs. (S35), (S36), (S38), and (S39) without environmental dissipation (i.e., $\kappa_a = \kappa_b = 0$), the poles equation (S47) can be further simplified as

$$\mathcal{D}(E_i) = [E_i - \Delta - g^2 G(x_{1,B}, x_{1,B}; E_i)]^2 - [g^2 G(x_{1,B}, x_{2,A}; E_i)]^2 = g^4 \prod_{p=\pm} [(E_i - \Delta)/g^2 - G_p(E_i)] = 0, \quad (\text{S49})$$

where

$$G_{\pm}(E_i) = G(x_{1,B}, x_{1,B}; E_i) \pm G(x_{1,B}, x_{2,A}; E_i) = - \frac{\sum_{p=\pm} [z \pm J F_{d+1}(y_p, -\delta)] p \Theta[p(1 - |y_+|)]}{\sqrt{z^4 - 4J^2 z^2 (1 + \delta^2) + 16J^4 \delta^2}} \Big|_{z=E_i}, \quad (\text{S50})$$

which satisfies $G_{\pm}(E_i) = -G_{\mp}(-E_i)$ since both y_{\pm} are even function with respect to z . To solve this poles equation, we first need to analyze the characteristics of $G_{\pm}(E_i)$ within the band-gap region and at the band edges. This analysis

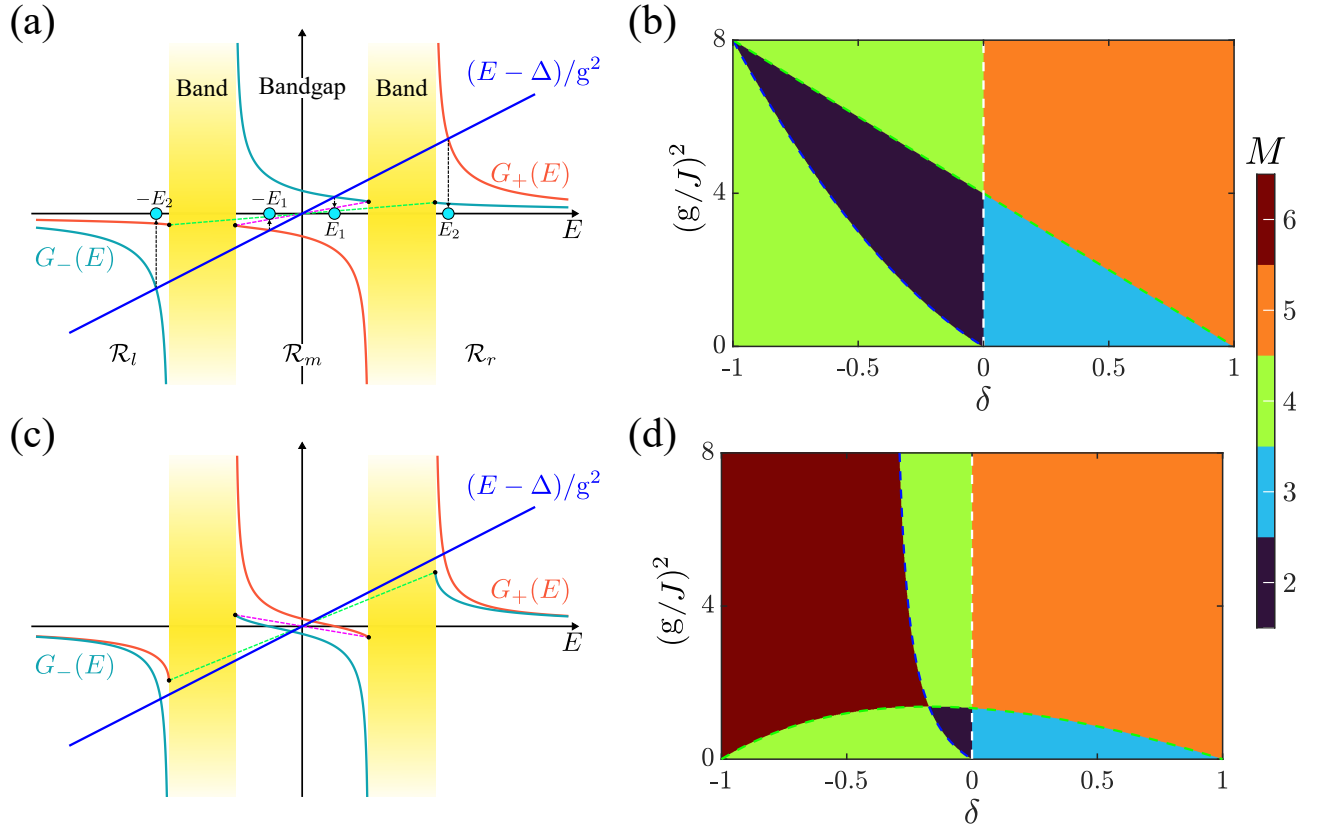


FIG. S5. Panels (a) and (c) describe the difference $G_{\pm}(E)$ as a function of E in the SHH environment, for $d = -1$ and $d = -2$ respectively. Roots of the poles equation (i.e., the BSEs) are obtained from the intersection points between $(E - \Delta)/g^2$ (blue solid line) and $G_{\pm}(E)$ (teal and orange solid lines). Panels (b) and (d) show the number of bound states M as a function of the dimerization parameter δ and the atom-bath coupling strength g , for $d = -1$ and $d = -2$ respectively. The blue and green dashed lines are given by Eq. (S63). Here, we focus on a non-dissipative environment, i.e., $\kappa_a = \kappa_b = 0$.

will help us determine the number of intersection points between $G_{\pm}(E_i)$ and $(E_i - \Delta)/g^2$, i.e., the number of bound states. For simplicity, we divide the bandgap into three intervals, i.e., $\mathcal{R}_l = (-\infty, -2J)$, $\mathcal{R}_m = (-2J|\delta|, 2J|\delta|)$, and $\mathcal{R}_r = (2J, +\infty)$. It is not difficult to observe that when $z \in \mathcal{R}_m$, $-1 < y_+ < 0$, while when $z \in \mathcal{R}_l \cup \mathcal{R}_r$, $y_+ > 1$.

First, we will start our analysis with the middle region of the bandgap \mathcal{R}_m , and we have

$$G_{\pm}(z) = \frac{-[z \pm JF_{d+1}(y_+, -\delta)]}{\sqrt{z^4 - 4J^2z^2(1 + \delta^2) + 16J^4\delta^2}} = -\frac{z \pm J[(1 - \delta)y_+^{|d+1|} + (1 + \delta)y_+^{|d|}]}{\sqrt{z^4 - 4J^2z^2(1 + \delta^2) + 16J^4\delta^2}} = -G_{\mp}(-z), \quad \text{for } z \in \mathcal{R}_m. \quad (\text{S51})$$

According to Eq. (S51), we only need to analyze the behavior of $G_+(z)$ because G_+ and G_- are mutually symmetric with respect to the ordinate origin, as shown in Figs. S5(a) and S5(c). Additionally, we find that $G_+(z)$ is a monotonic function with respect to z in the interval \mathcal{R}_m , i.e., $[dG_+/dz]_{z \in \mathcal{R}_m} < 0$. Finally, determining whether the number of bound states can be change abruptly mainly depends on the behavior (divergence or convergence) of $G_{\pm}(z)$ at the band edges. As $z \rightarrow \pm 2J|\delta|$, the denominator of $G_{\pm}(z)$ evidently approaches zero with a behavior proportional to $\sqrt{2J|\delta| \pm z}$. Thus, we only need to analyze the Taylor expansion of $F_{d+1}(y_+, -\delta)$ at $z = \pm 2J|\delta|$, i.e.,

$$F_{d+1}(y_+, -\delta)|_{z=\pm 2J|\delta|} = 2(-1)^d \left\{ \delta - \sqrt{\frac{|\delta|/J}{1 - \delta^2}} [\delta(|d| + |d+1|) + |d| - |d+1|] (2J|\delta| \pm z)^{\frac{1}{2}} \right\} + \mathcal{O}[(2J|\delta| \pm z)^{\frac{1}{2}}]. \quad (\text{S52})$$

By plugging Eq. (S52) into $G_+(z)$ in Eq. (S51), we have

$$\lim_{z \rightarrow \pm 2J|\delta|} G_+(z) = \frac{-1}{2J\sqrt{1 - \delta^2}} \lim_{z \rightarrow \pm 2J|\delta|} \frac{z + 2J(-1)^d \delta}{\sqrt{4J^2\delta^2 - z^2}} + \mathcal{G}_1(d, \delta), \quad (\text{S53})$$

where, for later convenience, we define

$$\mathcal{G}_1(d, \delta) = \frac{(-1)^{d+\Theta[d]}}{2J(1-\delta^2)} [1 - (2d+1)\delta]. \quad (\text{S54})$$

For the first term on the RHS of Eq. (S53), it is evident that different values of d and δ will yield distinctly different results, i.e.,

$$\lim_{z \rightarrow -2J|\delta|} \frac{z + 2J(-1)^d \delta}{\sqrt{4J^2 \delta^2 - z^2}} = \begin{cases} -\infty & \Theta[(-1)^d \delta] = 0 \\ 0 & \Theta[(-1)^d \delta] = 1 \end{cases}, \quad \lim_{z \rightarrow 2J|\delta|} \frac{z + 2J(-1)^d \delta}{\sqrt{4J^2 \delta^2 - z^2}} = \begin{cases} 0 & \Theta[(-1)^d \delta] = 0 \\ +\infty & \Theta[(-1)^d \delta] = 1 \end{cases}, \quad (\text{S55})$$

which result in

$$\lim_{z \rightarrow -2J|\delta|} G_+(z) = \begin{cases} +\infty & \Theta[(-1)^d \delta] = 0 \\ \mathcal{G}_1(d, \delta) & \Theta[(-1)^d \delta] = 1 \end{cases}, \quad \lim_{z \rightarrow 2J|\delta|} G_+(z) = \begin{cases} \mathcal{G}_1(d, \delta) & \Theta[(-1)^d \delta] = 0 \\ -\infty & \Theta[(-1)^d \delta] = 1 \end{cases}. \quad (\text{S56})$$

In addition, the difference $G_+(z) - G_-(z)$ also plays an important role in the analysis of the aforementioned intersection points. According to $\max(y_+) = y_+|_{z=0} = [(\delta-1)/(\delta+1)]^{\text{sign}(\delta)}$ and Eq. (S51), the difference is computed as

$$\begin{aligned} G_+(z) - G_-(z) &= G_+(z) + G_+(-z) = \frac{-2J[(1-\delta)y_+^{|d+1|} + (1+\delta)y_+^{|d|}]}{\sqrt{z^4 - 4J^2 z^2(1+\delta^2) + 16J^4 \delta^2}} \\ &= \begin{cases} 2J(1+\delta)y_+^{|d+1|} [\max(y_+)^{\text{sign}(\delta)} - y_+] & d \leq -1 \\ 2J(1-\delta)y_+^{|d|} [\max(y_+)^{\text{sign}(-\delta)} - y_+] & d \geq 0 \end{cases}. \end{aligned} \quad (\text{S57})$$

For given parameters δ and d , within the band-gap region \mathcal{R}_m , $G_+(z)$ is consistently positioned either entirely above or entirely below $G_-(z)$, and these two functions have a unique intersection point [i.e., $G_+(0) = G_-(0) = 0$] only when $d \leq -1 \wedge \delta > 0$ or $d \geq 0 \wedge \delta < 0$.

Second, for the other two band-gap regions, \mathcal{R}_l and \mathcal{R}_r , we also have

$$G_{\pm}(z) = \frac{z \pm JF_{d+1}(y_-, -\delta)}{\sqrt{z^4 - 4J^2 z^2(1+\delta^2) + 16J^4 \delta^2}} = \frac{z \pm J[(1-\delta)y_-^{|d+1|} + (1+\delta)y_-^{|d|}]}{\sqrt{z^4 - 4J^2 z^2(1+\delta^2) + 16J^4 \delta^2}}, \quad \text{for } z \in \mathcal{R}_l \cup \mathcal{R}_r. \quad (\text{S58})$$

Similarly, we only need to analyze the behavior of $G_{\pm}(z)$ in one of these regions due to $G_{\pm}(z) = -G_{\mp}(-z)$. As a consequence, we focus on the case of $z \in \mathcal{R}_r$. We find that $G_{\pm}(z)$ both are a monotonic function in the interval \mathcal{R}_l , i.e., $[dG_{\pm}/dz]_{z \in \mathcal{R}_r} < 0$, and the difference $G_+(z) - G_-(z)$ is always more than zero, i.e., $G_+(z) > G_-(z)$ for $z \in \mathcal{R}_r$. It is evident that when $z \rightarrow +\infty$, $G_{\pm}(z)$ both approach zero. As $z \rightarrow 2J$, the denominator of $G_{\pm}(z)$ evidently approaches zero with a behavior proportional to $\sqrt{z-2J}$. Thus, the Taylor expansion of $F_{d+1}(y_-, -\delta)$ at $z = 2J$ is given by

$$F_{d+1}(y_-, -\delta)|_{z=2J} = 2 - \frac{2[\delta(|d| - |d+1|) + |d| + |d+1|]}{\sqrt{J(1-\delta^2)}} (z-2J)^{\frac{1}{2}} + \mathcal{O}[(z-2J)^{\frac{3}{2}}]. \quad (\text{S59})$$

By plugging Eq. (S59) into $G_{\pm}(z)$ of Eq. (S58), we have

$$\lim_{z \rightarrow 2J} G_+(z) = +\infty, \quad \lim_{z \rightarrow 2J} G_-(z) = \mathcal{G}_2(d, \delta) \equiv \frac{(-1)^{\Theta[d]}[\delta - (2d+1)]}{2J(1-\delta^2)} > 0. \quad (\text{S60})$$

Now, as shown in Figs. S5(a) and S5(c), for $\Delta = 0$, we find that the critical point, where the number of intersection points (BSEs) between $(E - \Delta)/g^2$ and $G_{\pm}(E)$ undergoes an abrupt change, occurs then the slope of the blue solid line equals the slope the pink dashed line or the green dashed line. For the pink dashed line within the bandgap \mathcal{R}_m , according to Eq. (S56), its slope is given by

$$k_1 = (-1)^{\Theta[(-1)^d \delta]} \frac{\mathcal{G}_1(d, \delta) - [-\mathcal{G}_1(d, \delta)]}{2J|\delta| - [-2J|\delta|]} = \frac{(-1)^{\Theta[d]}[(2d+1)\delta - 1]}{4J^2 \delta(1-\delta^2)}. \quad (\text{S61})$$

Similarly, for the green dashed line, according to Eq. (S60), its slope is given by

$$k_2 = \frac{\mathcal{G}_2(d, \delta) - [-\mathcal{G}_2(d, \delta)]}{2J - [-2J]} = \frac{(-1)^{\Theta[d]}[\delta - (2d+1)]}{4J^2(1-\delta^2)}. \quad (\text{S62})$$

Thus, the two phase boundaries are given by

$$\ell_1 : k_1 = \frac{1}{g^2} \implies |g| = 2J \sqrt{\frac{(-1)^{\Theta[d]}\delta(1-\delta^2)}{(2d+1)\delta-1}}, \quad \ell_2 : k_2 = \frac{1}{g^2} \implies |g| = 2J \sqrt{\frac{(-1)^{\Theta[d]}(1-\delta^2)}{\delta-(2d+1)}}, \quad (\text{S63})$$

which recover Eq.(10) in the main text for $d < 0$ and the number of bound states changes in pairs on either side of these two phase boundaries. Additionally, when $d \leq -1 \wedge \delta > 0$ or $d \geq 0 \wedge \delta < 0$ are satisfied, the number of bound states also changes on either side of the topological phase boundary ($\delta = 0$) due to $G_{\pm}(E)|_{E=0} = 0$, but these changes do not occur in pairs, as shown in Figs. S5(b) and S5(d).

Finally, let us return to the long-time behavior of the maximum stored energy, i.e., $\max_t[\mathcal{E}(\infty)] = \omega_e \max_t[|c_B(\infty)|^2]$. After analyzing the situation of changes in the number of bound states, according to Eq. (S46), we also need to calculate the residues corresponding to these bound states, i.e., $\text{Res}[\mathcal{C}(z), E_i]$. When $d \leq -1 \wedge \delta > 0$ or $d \geq 0 \wedge \delta < 0$, based on the above discussion, we know that the number of bound states is odd. Among these, there must be a zero-energy bound state (corresponding to a second-order pole), and the remaining BSEs are non-zero and occur in pairs with opposite signs (corresponding to first-order pole). Meanwhile, the zero-energy bound-state residue equals zero due to $G(x_{1,B}, x_{2,A}; E_i = 0) = 0$, whereas the residues of the other bound states are non-zero due to $G(x_{1,B}, x_{2,A}; E_i \neq 0) \neq 0$, specifically given by:

$$\text{Res}[\mathcal{C}(z), E_i = 0] = 0, \quad \text{Res}[\mathcal{C}(z), E_i \neq 0] = -\text{Res}[\mathcal{C}(z), -E_i \neq 0] \neq 0. \quad (\text{S64})$$

The last term in Eq. (S64) also holds when the above condition ($d \leq -1 \wedge \delta > 0$ or $d \geq 0 \wedge \delta < 0$) is not satisfied. As a consequence, the maximum stored energy in the long-time limit is computed as

$$\max_t[\mathcal{E}(\infty)]/\omega_e = \max_t \left| \sum_{E_k \in \text{BSEs}} \text{Res}[\mathcal{C}(z), E_k] e^{-iE_k t} \right|^2 = \max_t \left| \sum_{E_i > 0} 2 \text{Res}[\mathcal{C}(z), E_i] \sin(E_i t) \right|^2, \quad (\text{S65})$$

which can reach values arbitrarily close to $4\{\sum_i |\text{Res}[\mathcal{C}(z), E_i]|\}^2$, where $E_i > 0$. Because these self-energies and their derivatives are continuous across different bandgaps (i.e., \mathcal{R}_i , \mathcal{R}_m , and \mathcal{R}_r), the residues corresponding to the bound-state energies distributed in these bandgaps should also be continuous. Furthermore, since dG_{\pm}/dz diverges at the band-gap edges, $\text{Res}[\mathcal{C}(z), E_i]$ approaches zero when the bound-state energy E_i is close to the band-gap edges. Therefore, integrating the above discussions and Eq. (S64), we conclude that the derivative of the maximum stored energy (itself is always continuous), $\max_t[\mathcal{E}(\infty)]$, remains continuous across the topological phase boundary, while it becomes discontinuous across the phase boundaries ℓ_1 and ℓ_2 . This conclusion explains the phenomenon shown in the insets of Fig.2(c) in the main text.

B. Dissipation immunity of quantum battery

For the configuration considered in Sec. S3A, as shown in Fig. S4, regardless of the distance between the quantum charger and QB, at the appropriate parameters, the quantum charger can always transfer almost all of its energy to QB through the topological environment, i.e., $\max_t[\mathcal{E}(\infty)]/\omega_e \approx 1$. However, once there is photon loss in the SSH photonic lattice, all the coherent bound states (i.e., $\text{Im}[E_i] = 0$) will transform into dissipative bound states (i.e., $\text{Im}[E_i] < 0$), and consequently, all the energy in the quantum charger and QB will be lost in the long-time limit, which implies $\mathcal{E}(\infty) = 0$. In fact, there exists another configuration with a dark state, different from configuration-I, whose energy transfer from the quantum charger to QB remains unaffected by the environmental dissipation, as shown in Fig. S6. For the configuration-II, the corresponding pole equation is given by

$$\mathcal{D}(E_i) = [E_i - \Delta - \Sigma_{11}^{AA}(E_i)]^2 - [\Omega + \Sigma_{11}^{AA}(E_i)]^2 = [E_i - \Delta - \Omega - 2 \times \Sigma_{11}^{AA}(E_i)][E_i - \Delta + \Omega] = 0 \quad (\text{S66})$$

with the single-emitter self-energy [see Eq. (S35)]

$$\Sigma_{11}^{AA}(z) = g^2 G(x_{1,A}, x_{1,A}; z) = -\frac{zg^2 \sum_{p=\pm} p \Theta[p(1-|\tilde{y}_+|)]}{\sqrt{z_{\text{nh}}^4 - 4J^2 z_{\text{nh}}^2 (1+\delta^2) + 16J^4 \delta^2}}, \quad (\text{S67})$$

where $z_{\text{nh}} = \sqrt{z(z+i\kappa/2)}$. According to the pole equation, it is evident that this dissipative system can have at most two coherent bound states. One is an environment-independent bound state, also known as the dark state, with

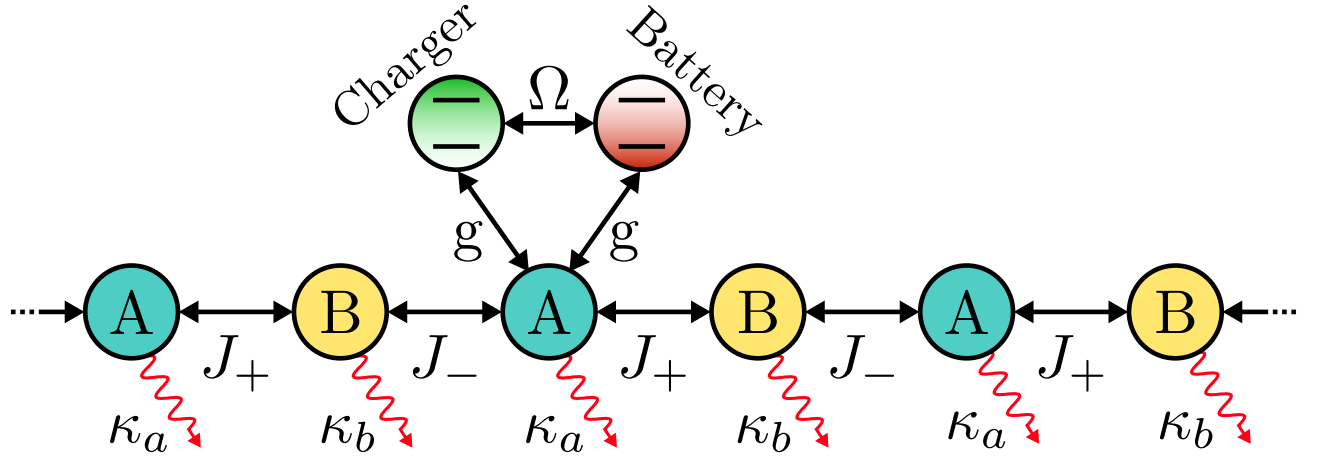


FIG. S6. Configuration-II: The quantum charger and the QB are located in the same sublattices at the same positions, i.e., $\alpha = \beta = A$ and $x_1 = x_2$, which means that the direct coupling interaction appears, i.e., $\Omega_{12}^{\alpha\beta} = \Omega \neq 0$. Here, κ_a (κ_b) is the decay rate of the sublattice A (B), and we assume that there exists a single-sublattice dissipation, i.e., $\kappa_a = \kappa \neq 0$ and $\kappa_b = 0$.

energy $E_{\text{dark}} = \Delta - \Omega$. The other, known as the vacancy-like dressed bound state [S7], appears only when $\Delta + \Omega = 0$, and has the energy $E_{\text{vbs}} = 0$. Subsequently, when $\Delta = -\Omega \neq 0$, the residues of these bound state are computed as

$$\text{Res}[\mathcal{C}(z), E_{\text{dark}}] = \frac{\Omega + \Sigma_{11}^{AA}(z)}{d\mathcal{D}(z)/dz} \Big|_{z=E_{\text{dark}}} = -\frac{1}{2}, \quad \text{Res}[\mathcal{C}(z), E_{\text{vbs}}] = \frac{\Omega + \Sigma_{11}^{AA}(z)}{d\mathcal{D}(z)/dz} \Big|_{z=E_{\text{vbs}}} = \frac{J^2|\delta|}{g^2 + 2J^2|\delta|}. \quad (\text{S68})$$

Besides, the dark state $|\psi_{\text{dark}}\rangle$ and the vacancy-like dressed bound state $|\psi_{\text{vbs}}\rangle$ can be obtained by solving the secular equation $H_{\text{eff}}|\psi\rangle = E|\psi\rangle$. Consequently, these bound states are derived as

$$|\psi_{\text{dark}}\rangle = \frac{1}{\sqrt{2}}(\sigma_+^{\text{C}} - \sigma_+^{\text{B}})|g, g; \text{vac}\rangle, \quad |\psi_{\text{vbs}}\rangle = \sqrt{\frac{2J^2|\delta|}{g^2 + 2J^2|\delta|}} \left[\frac{1}{\sqrt{2}}(\sigma_+^{\text{C}} + \sigma_+^{\text{B}}) + \sum_j (c_{j,a}a_j^\dagger + c_{j,b}b_j^\dagger) \right] |g, g; \text{vac}\rangle, \quad (\text{S69})$$

where

$$c_{j,a} = 0, \quad c_{j,b} = -\frac{\sqrt{2}g}{J(1+\delta)} \left(\frac{\delta-1}{\delta+1} \right)^{x_j-x_1} \text{sign}(\delta) \times \Theta[\delta(x_j - x_1 + 0^+)]. \quad (\text{S70})$$

Finally, combining Eqs. (S46) and (S68), the probability amplitude for QB to be in the excited state in the long-time limit is given by

$$c_{\text{B}}(\infty) = \frac{J^2|\delta|}{g^2 + 2J^2|\delta|} - \frac{1}{2}e^{2iGt}. \quad (\text{S71})$$

This formula shows beyond doubt that even in the dissipative environment, the energy in the quantum charger can always be transferred to QB, particularly in the case of weak coupling, i.e., $g \ll J$, and nearly all the energy can be transferred to QB. The two bound states play a crucial role in the energy transfer process. Additionally, according to the definition (9) in the main text, the maximum ergotropy is computed as

$$\max_t[\mathcal{W}(\infty)]/\omega_e = \max_t[2|c_{\text{B}}(\infty)|^2 - 1]\Theta[|c_{\text{B}}(\infty)|^2 - 1/2] = \frac{8J^4\delta^2 - g^4}{2(2J^2|\delta| + g^2)^2} \Theta\left(2^{\frac{3}{4}}J\sqrt{|\delta|} - |g|\right), \quad (\text{S72})$$

which supports Eq.(11) in the main text. We note that both of these bound states are essential; without either one, the maximum of the extractable energy would be zero in the long-time limit, i.e., $\max_t[\mathcal{W}(\infty)] = 0$.

C. The impact of environmental dissipation on quantum battery performance

Before proceeding, we turn to the pole equation (S66) and take $\Delta = -\Omega$, and the pole equation can be further simplified as

$$\mathcal{D}(E_i) = E_i(E_i + 2\Omega) \left[1 + \frac{g^2 \sum_{p=\pm} p \Theta[p(1 - |\tilde{y}_+|)]}{\sqrt{z_{\text{nh}}^4 + 4J^2 z_{\text{nh}}^2 (1 + \delta^2) + 16J^4 \delta^2}} \right]_{z=E_i} = 0. \quad (\text{S73})$$

Apart from the two coherent bound state mentioned in Sec. S3B, according to the pole equation, we can also find two dissipative bound states, and the corresponding energies can be obtained by solving

$$z_{\text{nh}}|_{z=E_i} = \pm \sqrt{2J^2(1 + \delta^2) + 2\sqrt{g^4 + J^4(1 - \delta)^2}} \equiv E_{0,\pm}, \quad (\text{S74})$$

where $E_{0,\pm}$ are the bound-state energies in the non-dissipative environment, which satisfy $\mathcal{D}(E_{0,\pm})|_{\kappa=0} = 0$. The solution in Eq. (S74) is given by

$$E_{\kappa,\pm} = -\frac{i}{4}\kappa \pm \sqrt{E_{0,\pm}^2 - (\kappa/4)^2}, \quad (\text{S75})$$

which represent the dissipative bound-state energies in the dissipative environment. Subsequently, let us analyze the dissipative bound state contributions in a short time when $\kappa/J \gg 1$. First, following the Eq. (S68), the corresponding residues are computed as

$$\text{Res}[\mathcal{D}(z), E_{\kappa,\pm}] = \frac{\Omega + \Sigma_{11}^{AA}(z)}{d\mathcal{D}(z)/dz} \Big|_{z=E_{\kappa,\pm}} = \frac{g^4}{E_{\kappa,\pm}(E_{\kappa,\pm} + i\kappa/4)[E_{0,\pm}^2 - 2J^2(1 + \delta^2)]}. \quad (\text{S76})$$

Second, when $\kappa/J \gg 1$, we have

$$E_{\kappa,\pm} = -\frac{i\kappa}{4} \left[1 \pm \sqrt{1 - (4E_{0,\pm}/\kappa)^2} \right] = -\frac{i\kappa}{4} \{ 1 \pm [1 - 8(E_{0,\pm}/\kappa)^2 + o(\kappa^{-2})] \} \approx -(1 \pm 1) \frac{i\kappa}{4} \pm \frac{2iE_{0,\pm}^2}{\kappa}, \quad (\text{S77})$$

and the corresponding residues are given by

$$\text{Res}[\mathcal{D}(z), E_{\kappa,+}] \approx \frac{g^4}{[E_{0,+}^2 - 2J^2(1 + \delta^2)](-i\kappa/2)(-i\kappa/2 + i\kappa/4)} = \frac{-8g^4}{[E_{0,+}^2 - 2J^2(1 + \delta^2)]\kappa^2}, \quad (\text{S78})$$

$$\text{Res}[\mathcal{D}(z), E_{\kappa,-}] \approx \frac{g^4}{[E_{0,+}^2 - 2J^2(1 + \delta^2)](-2iE_{0,-}^2/\kappa)(-2iE_{0,-}^2/\kappa + i\kappa/4)} \approx \frac{2g^4}{[E_{0,-}^2 - 2J^2(1 + \delta^2)]E_{0,-}^2}. \quad (\text{S79})$$

Consequently, the contribution of the dissipative bound states can be written as

$$c_{\text{B}}^{\text{DBS}}(t) = \sum_{p=\pm} \text{Res}[\mathcal{D}(z), E_{\kappa,p}] e^{-iE_{\kappa,p}t} \approx \frac{-8g^4 \exp[-\kappa t/2]}{[E_{0,+}^2 - 2J^2(1 + \delta^2)]\kappa^2} + \frac{2g^4 \exp[-2E_{0,-}^2 t/\kappa]}{[E_{0,+}^2 - 2J^2(1 + \delta^2)]E_{0,-}^2}. \quad (\text{S80})$$

Finally, when $t \ll \kappa$, the first term on the RHS of Eq. (S80) can be ignored, and $\exp[-2E_{0,-}^2 t/\kappa] \approx 1$ within the last term. Thus, according to Eq. (S76), we have

$$c_{\text{B}}^{\text{DBS}}(t) \approx \frac{2g^4}{[E_{0,+}^2 - 2J^2(1 + \delta^2)]E_{0,-}^2} = c_{\text{B}}^{\text{BS}}(t_n), \quad (\text{S81})$$

where $t_n = 2n\pi/E_{0,+}$ and $c_{\text{B}}^{\text{BS}}(t)$ represent the contribution of the coherent bound states with energies $E_{0,\pm}$ in the non-dissipative environment. In conclusion, as the dissipation κ increases, we find that the stroboscopic dynamics of the dissipative system revert to those of the non-dissipative system, thereby achieving immunity to the effects of dissipation in short time and enhancing the performance of QB. Note that the contributions from the branch cuts are generally small and, therefore, have not been discussed here.

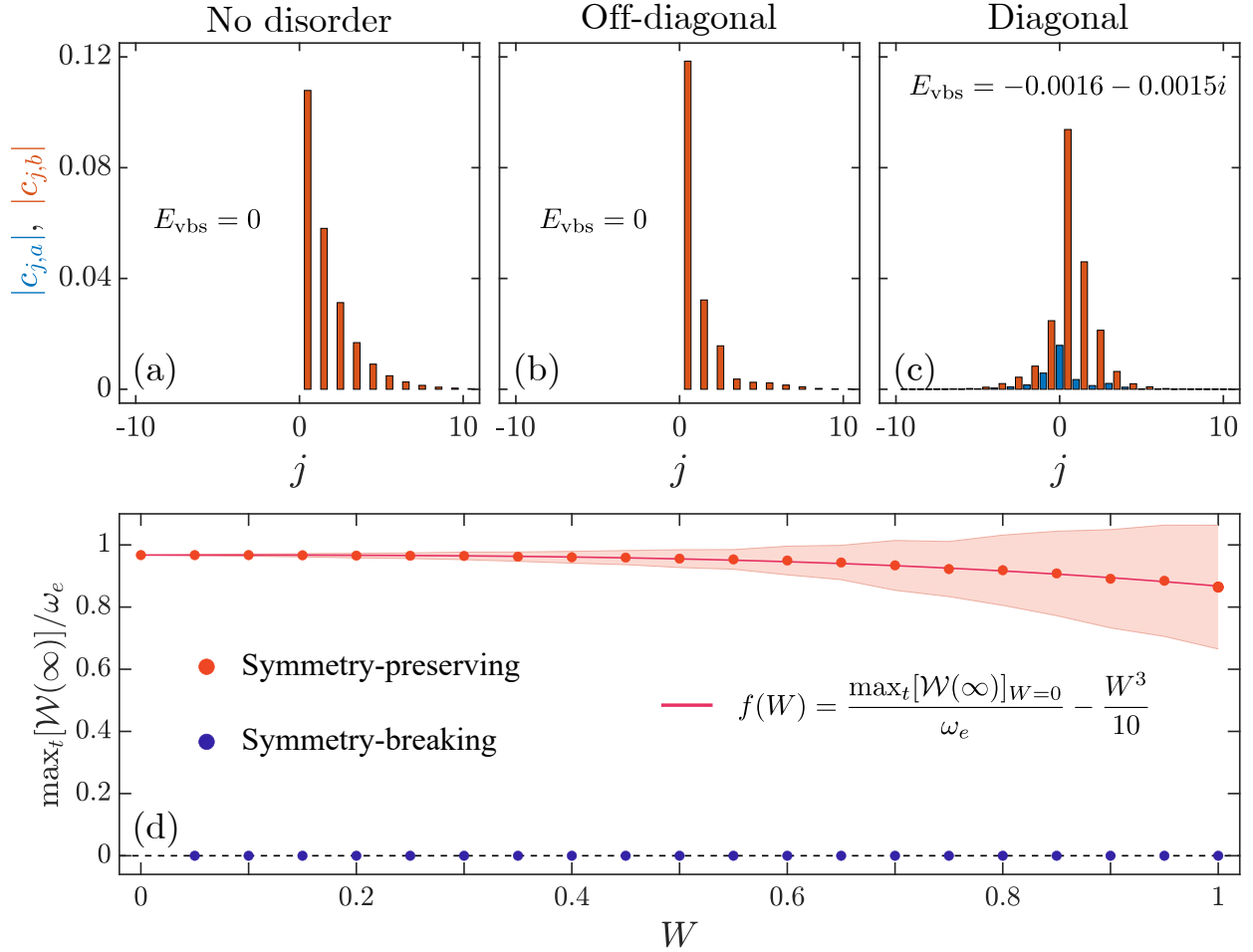


FIG. S7. Panels (a-c) describe the properties of the vacancy-like dressed bound state with and without disorder. The absolute value of probability amplitudes $|c_{j,a}|$ are shown in blue, while the $|c_{j,b}|$ are shown in orange. Panel (a) corresponds to the model without disorder, panel (b) corresponds to the model with disorder in the couplings between cavities, and panel (c) corresponds to the model with disorder in the resonant frequencies of cavities. The disorder strength is set to $W = 0.5$ in both cases with disorder. For each case, the value of the energy of the vacancy-like dressed bound state is shown at the inside of the plots, e.g., $E_{\text{vbs}} = 0$. Panel (d) shows the maximum ergotropy $\max_t[\mathcal{W}(\infty)]$ of QB for the two different models of disorder as a function of the disorder strength W . The red (blue) dots correspond to the average value computed with a total of 10^3 instances of disorder for the symmetry-preserving (symmetry-breaking) case, and the shadow areas span their corresponding standard deviation. The pink line represents a fit. In all plots, the system parameters are chosen to be $\delta = 0.3$, $g = 0.1J$, $\Delta = -\Omega = 0.2J$, $\kappa_a = 10J$, $\kappa_b = 0$, and $x_1 = x_2 = 0$.

S4. EFFECTS OF DISORDER

In practical physical systems, disorder is inevitable and has profound effects on the performance of quantum batteries. In this section, we will discuss in detail the manifestation of disorder in the one-dimensional SSH model and its impact on vacancy-like dressed bound state and the performance of quantum batteries, particularly focusing on ergotropy.

Here, we primarily investigate the impact of two types of disorder: one that affects the cavities' free frequencies (diagonal), and the other that affects the tunneling amplitudes between them (off-diagonal). The former corresponds to the addition of random diagonal terms to the bath's Hamiltonian, modifying it as $H_{\text{bath}} \rightarrow H_{\text{bath}} + \sum_j (\epsilon_{a,j} a_j^\dagger a_j + \epsilon_{b,j} b_j^\dagger b_j)$, thereby breaking the chiral symmetry of the original model. The latter corresponds to the addition of off-diagonal random terms, modifying the Hamiltonian as $H_{\text{bath}} \rightarrow H_{\text{bath}} + \sum_j (\epsilon_{1,j} a_j^\dagger b_j + \epsilon_{2,j} b_j^\dagger a_{j+1} + \text{H.c.})$, which preserves the chiral symmetry. We take the disorder parameters $\epsilon_{\nu,j}/J$ ($\nu = a, b, 1, 2$) from a uniform distribution

within the range $[-W, W]$ for each j th unit cell, where W represents the disorder strength. Additionally, we only focus on the configuration-II (see Fig. S6) and the maximum ergotropy. Therefore, as concluded in Sec. S3B, we know that even in the presence of sublattice dissipation, the energy in the quantum charger can be almost completely transferred to QB through the dissipative topological environment, primarily due to the contributions from the dark state and vacancy-like dressed bound state, i.e., Eq. (S69). We can be confident that the dark state is unaffected by above any type of disorder, due to the unique properties of the dark state, which decouple from the environment. Therefore, in the presence of disorder, the changes in the vacancy-like dressed bound state are the only factor influencing the performance of QB.

In the first row of Fig. S7, we plot the shape of the three vacancy-like dressed bound states for a situation without disorder and with off-diagonal (diagonal) disorder. Note that for the situation with diagonal disorder, although there is no vacancy-like dressed bound state, we still refer to it as such for convenience. For the symmetry-preserving case (i.e., no disorder or off-diagonal disorder), as shown in Figs. S7(a) and S7(b), we observe that the dressed bound state exhibits a unidirectional spatial profile and has components only on sublattice B. Additionally, compared to the clean system, in the case with off-diagonal disorder, the dressed bound-state energy remains zero, indicating that chiral symmetry ensures the presence of the dressed bound state, with slight changes in the absolute magnitude of the component of the bound state on sublattice B. In contrast, for the symmetry-breaking case (i.e., diagonal disorder), as shown in Fig. S7(c), we find that the state loses its unidirectional property and has a non-zero component on each sublattice. Furthermore, its energy also becomes a complex number with a non-zero imaginary part, i.e., $E_{\text{vbs}} = -0.0016 - 0.0015i$, indicating that breaking chiral symmetry disrupts the presence of the dressed bound state. Consequently, for our system, we can conclude that as long as chiral symmetry is preserved, even in the presence of disorder, the maximum ergotropy can remain high due to the contributions of the dark state and the vacancy-like dressed bound state. Conversely, when chiral symmetry is broken, resulting in the disappearance of the vacancy-like dressed bound state, the maximum ergotropy drops to zero. In fact, the data of these orange and blue dots in Fig. S7(c) corroborates this conclusion. More importantly, as shown by the orange dots in Fig. S7(c), we find that the maximum ergotropy is strongly robust to off-diagonal disorder. As disorder strength W increases, its average value obeys a power-law distribution, i.e., $f(W) = \max_t[\mathcal{W}(\infty)]_{W=0}/\omega_e - W^3/10$, where $\max_t[\mathcal{W}(\infty)]_{W=0}/\omega_e$ is given by Eq. (S72), as indicated by the pink line in Fig. S7(c). Even under strong off-diagonal disorder, such as $W = 1$, the average value of maximum ergotropy can still exceed 4/5. However, as shown by the blue dots in Fig. S7(c), the maximum ergotropy is always zero for the symmetry-breaking case.

* xinyoulu@hust.edu.cn

† c-shang@iis.u-tokyo.ac.jp

- [S1] C. Cohen-Tannoudji, J. Dupont-Roc, and G. Grynberg, *Atom-photon interactions: basic processes and applications* (John Wiley & Sons, 1998).
- [S2] W. P. Su, J. R. Schrieffer, and A. J. Heeger, Solitons in polyacetylene, *Phys. Rev. Lett.* **42**, 1698 (1979).
- [S3] Z. Gong, M. Bello, D. Malz, and F. K. Kunst, Anomalous behaviors of quantum emitters in non-hermitian baths, *Phys. Rev. Lett.* **129**, 223601 (2022).
- [S4] A. J. Daley, Quantum trajectories and open many-body quantum systems, *Advances in Physics* **63**, 77 (2014).
- [S5] A. Guo, G. J. Salamo, D. Duchesne, R. Morandotti, M. Volatier-Ravat, V. Aimez, G. A. Siviloglou, and D. N. Christodoulides, Observation of \mathcal{PT} -symmetry breaking in complex optical potentials, *Phys. Rev. Lett.* **103**, 093902 (2009).
- [S6] A. González-Tudela and J. I. Cirac, Non-Markovian Quantum Optics with Three-Dimensional State-Dependent Optical Lattices, *Quantum* **2**, 97 (2018).
- [S7] L. Leonforte, A. Carollo, and F. Ciccarello, Vacancy-like dressed states in topological waveguide qed, *Phys. Rev. Lett.* **126**, 063601 (2021).